NRL Report 6820

A Theoretical and Experimental Study of the AC Losses of a High Field Superconductor and the Implications for Power Applications

DONALD J. HANRAHAN

Electron Physics Branch
Electronics Division

February 26, 1969

NAVAL RESEARCH LABORATORY
Washington, D.C.

This document has been approved for public release and sale; its distribution is unlimited.

This report is a thesis that is being issued as a final report on NRL Problem E01-01, Projects RR 010-04-41-5950 (RN) and SR 007-12-01-0800. The manuscript was submitted for an NRL Report on October 14, 1968.

ABSTRACT

Title of Thesis: A Theoretical and Experimental Study of the AC Losses of a High Field Superconductor and the Implications for Power Applications

Donald J. Hanrahan, Doctor of Philosophy, February 1969

Thesis directed by: Assistant Professor Marshall D. Abrams

A theory for the hysteresis loss of a high-field superconductor carrying ac is presented, based on the Riemersma critical state model ($\mathbf{B} \times \mathbf{J} = \mathbf{C}$). Voltage waveforms, energy loss per cycle, and limiting values of effective resistivity are derived. For sinusoidal current of frequency f in 10-mil wire the high (critical) current limit of resistivity is found to be $4.06 \cdot 10^{-14}$ f (ohm-meter) compared to $0.93 \cdot 10^{-16}$ f for a current peak of one-tenth the critical current; both values are independent of the high-field material used. An equivalent circuit consisting of a variable inductance is proposed for the hysteretic superconductor and three possible definitions of the inductance are discussed. In any case, the inductance is nonlinear, a transcendental function of the current, the function being different on the four segments of a hysteresis loop. The high-current limit of the absolute, internal inductance (the preferred definition) per unit length is $\mu_0/3\pi$ (henry/meter).

Experiments were performed at 4.2°K on bifilar windings of 10-mil, Nb25%Zr wire, both bare and copper plated. Currents up to the critical value were used at frequencies of 60, 400, and 800 Hz. A compensation technique was employed to obtain the voltage due to internal magnetic field; oscillograms of the corresponding volt-amp characteristic and of various waveforms were made. Current and compensated voltage waveforms were used to calculate the loss per cycle. Oscillograms were in fair agreement with theoretical waveforms. Critical currents decreased with frequency, and the copper-plated wire had consistently higher values than the bare wire, although losses were higher for the copper-plated wire. There was some quantitative agreement between the experimental plated-wire loss and that calculated from the theory, but the measured bare-wire loss was generally less than that predicted by the theory, based on a measured critical current. The effective resistivity was found to vary as $f^{0.63}$, which fits neither an eddy-current theory nor the simple hysteresis model used. Experimental values of resistivity agree

more with Zar than with Wisseman. The theory gives a generally conservative estimate of the ac loss, useful for engineering purposes.

The feasibility of applying superconductivity to two classes of ac power equipment is discussed: (1) conventional apparatus such as transformers and rotating machines, already highly efficient, and (2) low-voltage static inverters which are not so efficient. A novel circuit is presented for a superconducting inverter or oscillator. We conclude in both cases that, although the superconducting device is more efficient than its room-temperature counterpart, the inefficiency of liquid-helium refrigeration precludes economical application of superconductivity. Unless new materials are developed that have either significantly higher transition temperatures or much less ac loss under high field conditions, the prospects for continuous ac power applications of superconductivity are bleak. There is still some promise for dc power applications and dc energy storage for discharge into pulse power devices.

ACKNOWLEDGMENT

I thank the Naval Research Laboratory for supporting my graduate studies with a Thomas A. Edison Memorial Fellowship, providing the environment which suggested the investigation, making available the library, laboratory, and computer facilities for carrying it out, and performing the secretarial, editorial, illustration, and reproduction services for this thesis. I am particularly indebted to the following individuals at NRL: S. C. Parker for preparation of the specimens, R. O. Pilon for inductance measurements, P. I. Peterson for invaluable experimental assistance, W. K. Gardner for analog to digital conversion of data, E. B. Wright for computer solutions and the limiting values of the loss expression, and D. S. Toffolo, B. J. Wilson and R. A. Hein for helpful discussions. Finally, I thank my advisor, Professor M. D. Abrams for his guidance and encouragement.

TABLE OF CONTENTS

Section	Page
ACKNOWLEDGMENT	iii
I. INTRODUCTION	1
A. Motivation	1
B. Types of Superconductors	4
C. Type III Superconductor Models	7
1. The Sponge Model	7
2. The Flux Pinning Model	7
D. AC Losses of Superconductors	9
1. Eddy-Current Loss	9
2. Hysteresis Loss	10
II. THEORY	12
A. The Initial Excitation	12
1. The Induced Voltage	14
B. The Hysteresis Loop	16
1. The Voltage Equations	16
2. The Loss per Cycle	22
3. The Effective Resistivity	24
C. An Equivalent Circuit	24
III. THE EXPERIMENT	27
A. The Specimens	27
B. The Circuit	28
1. The Compensation Method	28
2. Instrumentation	31
C. Procedure	31
1. Reduction of Data	34
D. Discussion of Results	34
1. Waveforms	34
2. Critical Current	36
3. AC Loss	38
IV. CONCLUSIONS	44
APPENDIX A – LIMITING VALUES OF THE LOSS EXPRESSION	47
APPENDIX B – THREE KINDS OF INDUCTANCE	49
APPENDIX C – SPECIMEN INDUCTANCE	52
WORKS CITED	54

LIST OF TABLES

Table		Page
1.	Absolute, Internal Inductances and Induced Voltages	26
2.	Bare Wire Critical DC Measurements	37

LIST OF FIGURES

Figure	Page
1. Basic superconducting inverter circuit	2
2. Astable multivibrator type of superconducting inverter or oscillator	3
3. Magnetization curve of a type I superconductor	5
4. Magnetization curve of a type II superconductor	5
5. Magnetization curves for (a) a type II superconductor, (b) the same material cold worked, and (c) the same material severely cold worked. (After Lowell (23).) The materials represented by (b) and (c) have become type III superconductors	6
6. Critical current curves corresponding to cases (a), (b), and (c) of Fig. 5. (After Lowell (23).)	6
7. Magnetic field (B) and current density (J) distributions in the cross-section of an infinite slab of type III superconductor according to the Bean model. An external, parallel field is applied to the virgin slab in (a) and removed in (b). (After Bean (25).)	7
8. Structure of a fluxoid in the mixed state of a type II or III superconductor. (After deGennes (21).) The fluxoid is depicted as a vortex of current (a) with the radial dependence of variables shown in (b). The normal core radius is ξ, the coherence length; n_s is the number of superconducting electrons per unit volume, and λ is the penetration depth	8
9. Flux-flow voltage across a current-carrying type II superconductor in the mixed state or type III superconductor when the critical state is exceeded. The Lorentz force F is supposed to cause the flux flow	9

LIST OF FIGURES–Continued

Figure		Page
10.	Equivalent circuit for eddy-current losses in the two-fluid model of a superconductor. (After Zar (15).) The superconducting component I_s takes a zero resistance path of inductance L_s while the normal component I_n takes a path of resistance R_n and inductance L_n. The two paths are coupled by mutual inductance M	10
11.	Portion of a long type-III superconductor carrying an alternating transport current (I) such that penetration of current density (**J**), magnetic induction (**B**), and electric field (**E**) occurs to a radius ρ, causing a surface voltage drop V	13
12.	Distribution of magnetic field and current density during initial excitation of the superconductor in Fig. 11	14
13.	Field and current distribution in the superconductor of Fig. 11 when $\dot{I} < 0$ and $0 < I < I_m$	16
14.	Field and current distribution in the superconductor of Fig. 11 when $\dot{I} < 0$ and $I = 0$	18
15.	Field and current distribution in the superconductor of Fig. 11 when $\dot{I} < 0$ and $I < 0$	19
16.	Initial excitation curve and major hysteresis loop in the $\varphi - I$ plane for the superconductor of Fig. 11	20
17.	Predicted voltage waveforms for a half cycle of sinusoidal current having various ratios of I_c/I_m in a type III superconductor	21
18.	Predicted voltage waveforms for a half cycle of triangular current having various ratios of I_c/I_m in a type III superconductor	21
19.	Predicted volt-amp characteristic for a sinusoidal current of a particular I_c/I_m ratio in a type III superconductor	22
20.	Predicted hysteresis loss per cycle for a type III superconductor	23

LIST OF FIGURES–Continued

Figure	Page
21. A specimen with current and voltage leads	28
22. A specimen undergoing test	29
23. Variable inductor used for compensation	29
24. Use of a variable mutual inductor to nullify the undesired portion of the specimen voltage. The specimen has an apparent inductance L_s, of which L_a is due to internal magnetic flux and L_0 is the remainder	30
25. Circuit diagram of the experimental arrangement	32
26. View of Variac, 120:6-V transformer, clamp-on ammeter, shunt, and switches	32
27. A general view of the experimental arrangement	33
28. Experimental waveforms of I, V, and $\int V\,dt$ for the plated wire at 800 Hz and I_m = 76.7 A. The voltage scale is 50 mV/cm	34
29. Experimental volt-amp characteristic of the plated wire at 800 Hz and I_m = 76.7 A. The voltage scale is 50 mV/cm	35
30. Critical currents versus frequency	36
31. Bare wire energy loss per cycle (15 April data) versus current amplitude compared to the calculated hysteresis loss for a critical current of 90 A	38
32. Bare wire energy loss per cycle (19 April data) versus current amplitude compared to the calculated hysteresis loss for a critical current of 90 A	39
33. Plated wire energy loss per cycle versus current amplitude compared to the calculated hysteresis loss for a critical current of 128 A	40
34. Bare wire power loss versus effective current	41
35. Plated wire power loss versus effective current	41
36. Bare wire effective resistivity versus effective current	41
37. Plated wire effective resistivity versus effective current	42
38. Bare wire effective resistivity versus frequency at an effective current of 50 A	43

I. INTRODUCTION

A. Motivation

The dc resistance of a superconductor in a weak magnetic field below its transition temperature is so low that it has never been measured. It is usually assumed to be zero (1). Shortly after his discovery of superconductivity in 1911, Kammerlingh Onnes visualized electromagnets wound of superconducting wire that would produce fields of 100 kilogauss or more. He soon found, however, that the resistance of the superconductors he was using became normal in a magnetic field of only a few hundred gauss. Superconducting magnets remained a dream until 1961 when the Bell Telephone Laboratories (2) announced that the compound Nb_3Sn remained superconducting in a field of 88 kilogauss. Since then other so-called high-field materials have been developed and many superconducting magnets have been built. There are still problems to be solved, but there is no doubt about the successful application of superconductivity to high-field electromagnets.

The advent of the high-field materials also reawakened interest in such power applications of superconductivity as motors, generators, transformers and transmission lines (3). Almost all electric machinery is electromagnetic in nature, i.e., operates by means of coupled circuits of electric current and magnetic flux. For a given rating the volume of a machine is inversely proportional to the product of current density and flux density (4). In conventional apparatus the material media for electric current and magnetic flux are copper and iron, respectively. Energy loss occurs in both: resistance loss in the copper, hysteresis and eddy-current losses in the iron. In a well-designed transformer, copper and iron losses are equal at full load (5).

If superconductors really had zero resistance, their use in electrical apparatus would avoid ohmic loss. Furthermore, the high-field materials remain superconducting at such high magnetic fields (over 100 kG) that iron would be saturated, so magnetic losses might also be avoided by using an air core. The use of high magnetic fields would reduce the volume required, as would the high current density (10^5 A/cm^2 or more) allowed in high-field materials (6). Some have estimated (7) that superconducting machinery including a refrigerator may be designed with a weight and volume of less than one-tenth that of conventional machinery.

Another possible power application of superconductivity is in a low-voltage, static inverter. In recent years there has been a great interest in direct-conversion schemes for the generation of electricity (8). These avoid the mechanical link and in some cases even

the thermal link involved in the usual central station process, which is duplicated in engine-generator sets for many mobile applications. Devices in the first category are thermoelectric, thermionic, and magnetohydrodynamic generators; examples of the second are solar cells, fuel cells, and radioactive batteries. Now all direct-conversion generators are inherently dc sources, whereas most utilization equipment requires an ac supply. Even dc loads will generally operate at a different voltage than that generated, necessitating an ac link for transformation. Furthermore, most direct-conversion generators are inherently low-voltage sources. Series arrangements tend to reduce system reliability, so a low-voltage static inverter is desirable.

Static inverters presently employ semiconductor switching elements such as silicon controlled rectifiers (9), tunnel diodes (10), and transistors (11), of which the last two are most useful for low-voltage inversion. These devices have significant forward voltage drops in the "closed position" which reduce their efficiency as input voltage is lowered. A typical tunnel diode has a 50-mV drop at 100 A, and a transistor is now available with a 70-mV drop at 200 A. In contrast to these figures, a closed superconducting switch would ideally have a voltage drop of zero, and is therefore, in principle at least, the answer to the low-voltage inverter problem.

A power cryotron (12) suggests itself as the superconducting switch. This might consist of a gate winding of the alloy Nb–Zr and a control winding of higher field material such as Nb_3Sn. Sufficient current in the control winding would drive the gate winding normal, thereby opening the switch. A basic superconducting inverter circuit is shown in Fig. 1 where only the two cryotrons need be in a cryogenic environment. The gate windings are shown as variable resistance elements r_1 and r_2. The control windings might be driven by a transistor oscillator circuit.

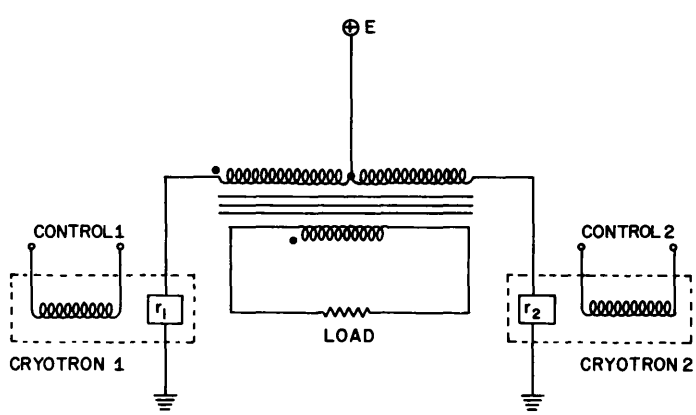

Fig. 1 – Basic superconducting inverter circuit

A self oscillating or Eccles-Jordan type of circuit proposed by the author is shown in Fig. 2. Resistors R_L represent a transformer-coupled load. A bias is established in each cryotron by current through windings marked L_3 so that gate windings r_1 and r_2 are just normal. Then if r_1 is made superconducting, voltage V_1 vanishes and capacitor C begins to charge with I_5 in the direction shown. This is in a direction to keep r_1 superconducting and r_2 normal. When C discharges, conditions are reversed so that the circuit oscillates as an astable multivibrator. It can be made more efficient if permanent magnets are used to provide the bias.

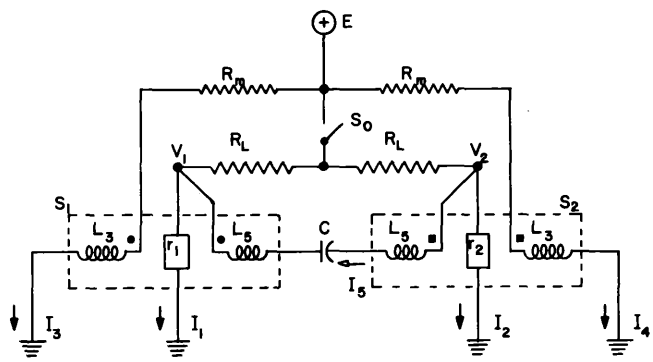

Fig. 2 – Astable multivibrator type of superconducting inverter or oscillator

The above discussion suggests that the prospects for power applications of superconductivity are bright. However almost every conceivable power application involves transient or alternating current. And superconductors have an effective ac resistance at any temperature above 0°K. For weak magnetic fields and frequencies up to 10 MHz the resistance is zero within experimental accuracy (13). But high-field superconductors at useful current levels have a measurable resistance at power frequencies. The significance of this fact lies in the inefficiency of refrigeration at superconducting temperatures. The Carnot efficiency of a heat pump working between 300 and 4°K is only 1.35%. Moreover, the state of the refrigeration art is such that only one-twelfth of the Carnot value is achieved (14). Thus a rule of thumb is that nearly 1 kW of refrigeration power is required for every watt dissipated at liquid helium temperature.

Therefore the prospects for power applications of superconductivity depend upon the amount of ac loss occurring in available, high-field materials. Even the high-field magnets already in operation—a dc application—are limited in their performance by ac effects; e.g., if charged too quickly they are driven normal. Unfortunately there is little agreement in the literature on the ac losses of high-field superconductors. Two papers report effective

resistivities for the popular Nb–25% Zr, 10-mil wire at 100 Hz that differ by nearly five orders of magnitude. Zar (15) reports $\rho = 1.5 \times 10^{-10}$ ohm-cm for currents up to 30 A; Wisseman *et al.* (16) report $\rho = 3 \times 10^{-15}$ ohm-cm for a peak current of about 8 A. In light of copper's room temperature resistivity of about 1.7×10^{-6} ohm-cm, the refrigeration efficiency of about 10^{-3} mentioned above, and the inevitable heat leaks of a cryogenic system, it is clear that the prospects for power applications of superconductivity depend upon whether Zar's or Wisseman's values are closer to what may be expected. The first purpose of this investigation was to answer that question.

This thesis presents a theoretical study of the bulk hysteresis loss in a high-field superconductor based on a simple critical state model. Riemersma (17) applied the model to an infinite slab in a uniform, constant applied field, with and without a static transport current, in order to determine the magnetization curve. We apply it to a long, cylindrical wire carrying an alternating transport current in its self field. Voltage waveforms, energy loss per cycle, and limiting values of effective resistivity are derived; an equivalent circuit based on variable inductance is proposed. The theoretical study is supplemented by an experimental investigation of voltage waveforms and deduced loss for Nb–25% Zr, 10-mil wire in a bifilar winding that approximates the geometry studied. Because of the interest in composite conductors for stabilization (18), both bare and copper-plated samples were tested. Measurements were made at 4.2°K for sinusoidal current up to the critical value at 60, 400, and 800 Hz. Experimental results are examined in light of both the theory presented and other published work. Finally, the implications for power applications of superconductivity are discussed and some recommendations made.

B. Types of Superconductors

Superconductivity is a quite general phenomenon. In 1963 Roberts (19) listed over 900 superconducting elements, compounds, and alloys with transition temperatures ranging from 0.07° to 18.5°K. Following a recent trend (20), we distinguish three types of superconductors on the basis of their magnetization curves. A perfect Meissner effect (1), i.e., complete flux exclusion, is expressed in mks units as

$$\mathbf{B} = \mu_0 (\mathbf{H} + \mathbf{M}) = 0 \tag{1}$$

where $\mathbf{B}$ is magnetic induction, μ_0 the permeability of free space, $\mathbf{H}$ the magnetic field intensity, and $\mathbf{M}$ the magnetization or magnetic moment per unit volume. This may be interpreted as either $\mathbf{H} = \mathbf{M} = 0$ or $\mathbf{M} = -\mathbf{H}$ within the body. Externally the representations

are equivalent. Internally the first is supposed to be physically correct, but the second is often convenient, e.g., in thermodynamic treatments, and leads to the plotting of magnetization curves. Even with the first interpretation the body exhibits a magnetic moment which may be attributed to an equivalent magnetization. In any case, the three types of superconductors are defined according to their magnetization curves as follows.

Figure 3 shows the magnetization curve for a long, cylindrical, type I superconductor in a long solenoid. Except for possible surface effects, the Meissner effect for a pure specimen is complete and the magnetic transition is abrupt at a critical field H_c. The magnetization curve for a type II superconductor in the same geometry is shown in Fig. 4.

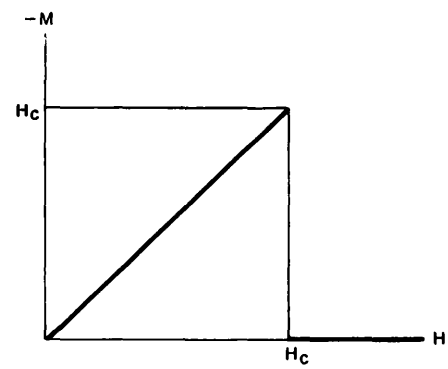

Fig. 3 – Magnetization curve of a type I superconductor

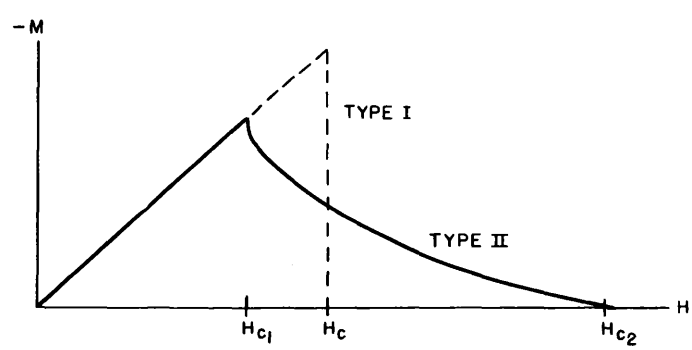

Fig. 4 – Magnetization curve of a type II superconductor

The material behaves as type I and is said to be in the Meissner state for fields below a lower critical field H_{c1}. Between H_{c1} and an upper critical field H_{c2} the material is in the so-called mixed state where there is progressive penetration of field until, except for surface effects (21), the specimen goes normal at H_{c2}. We call a superconductor type II if, and only if, it exhibits a *reversible* magnetization curve of the kind shown in Fig. 4. Type II superconductors generally have H_{c2} values higher than the H_c values of type I materials, which would appear to make them more attractive than type I materials for

power applications. But it has been shown (22) that a type II superconductor has a dc loss for currents producing a surface field greater than H_{c1}, and H_{c1} is generally less than H_c for a type I material.

Figure 5 shows magnetization curves for a type II superconductor, (a), and type III superconductors, (b) and (c), obtained from the material of (a) by cold working (23). The magnetization curve for a type III superconductor is similar to that of a type II for an initial increase of field but exhibits hysteresis for a subsequent reduction in field. Correlated with the appearance of hysteresis is a greatly enhanced critical current, as shown in Fig. 6. In contrast to type II, type III superconductors carry lossless dc in the mixed state, and some of them are the "new, high-field materials" so promising for applications. Of these materials the alloy Nb–Zr has been much used in superconducting magnets.

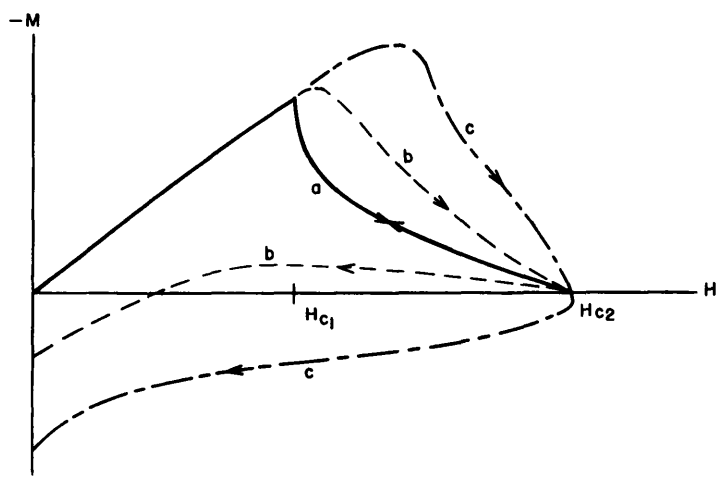

Fig. 5 – Magnetization curves for (a) a type II superconductor, (b) the same material cold worked, and (c) the same material severely cold worked. (After Lowell (23).) The materials represented by (b) and (c) have become type III superconductors

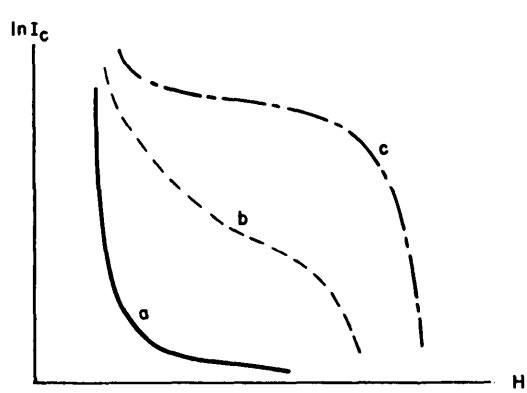

Fig. 6 – Critical current curves corresponding to cases (a), (b), and (c) of Fig. 5. (After Lowell (23).)

C. Type III Superconductor Models

Two models have been proposed to account for hysteresis in the magnetization curve and the current carrying capability of type III superconductors.

1. **The Sponge Model.** The sponge model was suggested by Mendelssohn (24) as early as 1935 to explain the behavior of "hard superconductors." The sponge structure consists of multiply-connected filamentary regions having a higher critical field than that of the matrix. Hysteresis occurs because supercurrents in the sponge meshes shield out an increasing field and trap flux in the interstices when the field is decreasing. Since the filaments are assumed to be interconnected, they permit a superconducting transport current despite field penetration.

The magnetic properties of this kind of structure have been calculated by Bean (25). He assumes a critical current density J_c independent of field, and that any emf, however small, will induce this full value to flow locally. The result for an infinite slab is shown in Fig. 7 for (a) an external, parallel field increased from zero to B_0 and (b) the external field removed. He is able to trace an entire hysteresis loop by this model, obtaining the diamagnetic equivalent of the Rayleigh hysteresis loop used in ferromagnetism (26).

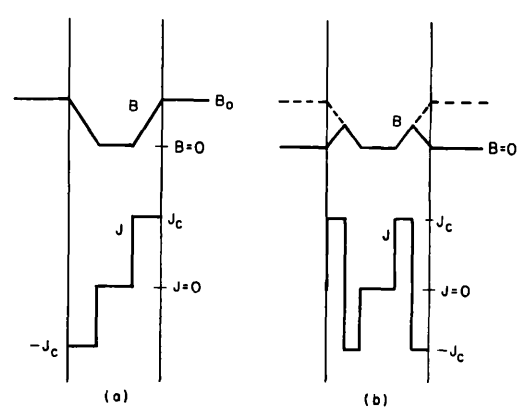

Fig. 7 – Magnetic field (B) and current density (J) distributions in the cross-section of an infinite slab of type III superconductor according to the Bean model. An external, parallel field is applied to the virgin slab in (a) and removed in (b). (After Bean (25).)

This theory predicts a size-dependent magnetization curve similar to those of type III superconductors. But critical current considerations (27) would have filaments make up a small fraction of the sample, while specific heat measurements (28) indicate that a large fraction of the material remains superconducting in high fields.

2. **The Flux Pinning Model.** According to the Abrikosov theory of type II superconductors (29), in the mixed state flux penetrates the specimen in vortices of circulating supercurrents called fluxoids. The structure of a fluxoid is indicated in Fig. 8. (Goodman (30) obtained results similar to those of Abrikosov in a system of alternating normal

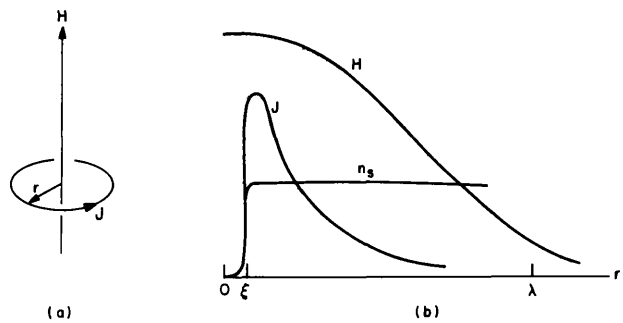

Fig. 8 – Structure of a fluxoid in the mixed state of a type II or III superconductor. (After deGennes (21).) The fluxoid is depicted as a vortex of current (a) with the radial dependence of variables shown in (b). The normal core radius is ξ, the coherence length; n_s is the number of superconducting electrons per unit volume, and λ is the penetration depth

and superconducting laminae, but there is a great deal of experimental evidence in support of the Abrikosov model (31).) There is a repulsive force among fluxoids, but in a uniform field the net magnetic force on any fluxoid vanishes, and the situation is stable. If the field becomes nonuniform by introduction of a transport current, the resulting pressure gradient causes the fluxoids to move. This is called flux flow and is supposed to be responsible for the dc resistance of type II superconductors in the mixed state.

Abrikosov pointed out, however, that lattice imperfections of various kinds tend to "pin down" the flux lines. This idea has been developed (32) to explain the high-field, transport current capability of type III superconductors. The pinning force on a fluxoid, or bundle of fluxoids, is due to a spatial variation of the free energy; hollows of the free energy occur at so-called pinning centers, which may be cavities, dislocations, precipitates, etc. The force tending to move the flux is interpreted as a Lorentz force, and the "critical state" of a type III superconductor is exceeded when the pinning force is overcome by the Lorentz force. Indeed, according to the "flux creep" theory of Anderson (33), even below this threshold, flux lines move slowly past the pinning centers because of thermal activation. The time decay of a persistent current has been observed (34) which is in agreement with the flux-creep theory, although it was estimated that complete decay would take 3×10^{92} years. When the critical state is exceeded, there is a gradual increase of apparent resistance, culminating in the normal value, over a range of current or magnetic field which is explained by the flux-flow theory of Kim, *et al.* (35).

Figure 9 represents a type III superconductor carrying a static transport current in the presence of a constant, applied field when the critical state is exceeded (or a type II superconductor under the same conditions in the mixed state). A voltage appears with the polarity of an IR drop, but it is attributed to an emf induced by flux flow. There has been much discussion (36) of the consistency of this interpretation with Maxwell's equations, but flux flow has been demonstrated (37) by the appearance of a similar voltage in a second specimen magnetically coupled to the first. Whatever the mechanism, the voltage drop (in the primary) indicates dissipation; the effect is equivalent to resistance.

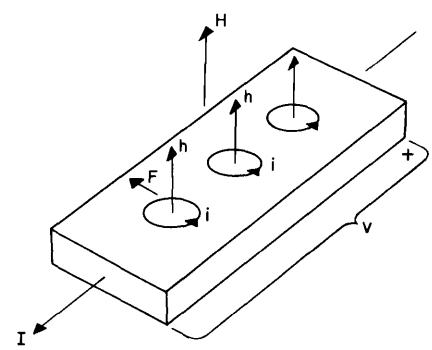

Fig. 9 – Flux-flow voltage across a current-carrying type II superconductor in the mixed state or type III superconductor when the critical state is exceeded. The Lorentz force **F** is supposed to cause the flux flow

D. AC Losses of Superconductors

1. **Eddy-Current Loss.** The dc resistance of any type of superconductor in a weak magnetic field below the transition temperature has never been detected. Quinn and Iffner (38) have set an upper limit of 10^{-23} ohm-cm on the resistivity. On the other hand, there is no appreciable change in reflectivity either in the visible or the near infrared during a superconducting transition (39), indicating no change in electrical properties at optical frequencies. Microwave and far infrared measurements (40) have been explained in terms of an electronic energy gap and correlated with perfect conductivity and the Meissner effect in the low-frequency limit. At 0°K the energy gap, written $2\Delta(0)$, can be characterized by a frequency f_g such that $hf_g = 2\Delta(0)$, where h is Planck's constant. The BCS theory (41) gives an expression for $\Delta(0)$ that puts f_g in the infrared. At 0°K the resistivity of a superconductor should be zero for all frequencies below f_g. But at higher temperatures, according to the two-fluid model (1), a fraction of the conduction electrons are "normal electrons," constituting a lossy secondary winding coupled to the "superconducting electrons." Thus an eddy current loss is theoretically present at any finite temperature and frequency.

A simple equivalent circuit proposed by Woodson and published by Zar (15) for the two-fluid model is shown in Fig. 10. The total current consists of a superconducting

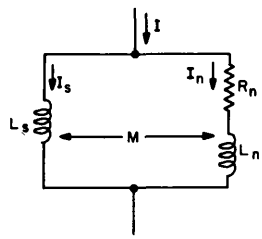

Fig. 10 – Equivalent circuit for eddy-current losses in the two-fluid model of a superconductor. (After Zar (15).) The superconducting component I_s takes a zero resistance path of inductance L_s while the normal component I_n takes a path of resistance R_n and inductance L_n. The two paths are coupled by mutual inductance M

component which takes a zero resistance path of inductance L_s and a normal component which takes a path of resistance R_n and inductance L_n; the two paths are coupled with mutual inductance M. Zar has shown that the admittance is

$$Y = \frac{R_n + j\omega (L_n + L_s - 2M)}{\omega^2 (M^2 - L_n L_s) + j\omega L_s R_n} . \tag{2}$$

This reduces to a pure susceptance if I_n and I_s have the same distribution within the superconductor or if I_s is confined to the surface. When I_s flows in a small penetration depth, a resistance appears which is approximately

$$R_{ac} = \frac{\omega^2 (L_s - M)^2}{R_n} . \tag{3}$$

For power frequencies R_n may be considered constant; then Eq. (3) shows the frequency-squared dependence which is characteristic of eddy-current losses. This kind of model should account for the ac loss at power frequencies of type I superconductors in fields less than H_c as well as that of type II and III superconductors in fields less than H_{c1}. For a type I superconductor at high frequencies, both classical and anomalous skin effect analyses (13) (where $R_n \propto \omega^{1/2}$ and $\omega^{2/3}$, respectively) at microwave frequencies also lead to $R_{ac} \propto \omega^2$. This surprising result should also apply to a type II or III superconductor in fields below H_{c1}.

2. **Hysteresis Loss.** In addition to the eddy-current loss contributed by the normal fluid, type III superconductors have a hysteresis loss in the mixed state. This loss was first calculated by Bean, who now believes his treatment to be valid for the flux-pinning model as well as the sponge model (25). He obtained a cubic dependence of loss on field strength. London (42) obtained similar results by the same means. In contrast to what we will call the Bean-London model, which has J_c independent of field, Kim *et al.* (34) have proposed the relation

$$a/J_c = B_0 + B \tag{4}$$

for the critical state, a and B_0 being constant. Fietz *et al.* (43) obtained a remarkably good fit to their data for Nb–25% Zr wire with

$$J_c = (a_0/b_0) \exp(-B/b_0) + c_0, \tag{5}$$

where a_0, b_0, and c_0 are constants. This form has no recognized physical significance. However they report a good fit to Eq. (4) with applied fields between 4 and 16 kilogauss, and that J_c is nearly independent of B for fields between 16 and 40 kilogauss. The reasonableness of these two approximations is suggested by the form of curve (c) in Fig. 6.

Riemersma (17) has used a critical state model in which

$$\mathbf{B} \times \mathbf{J} = \mathbf{C} \tag{6}$$

where $\mathbf{C}$ is a vector constant. He justifies this on the basis that the second term on the right-hand side of Eq. (4) represents a Lorentz force, whereas the physical significance of the first is unknown.

The Bean-London, Kim, and Riemersma models, whether thought of as representing a sponge structure or pinned flux, attribute the irreversible behavior of type III superconductors to bulk properties. On the other hand, Buchhold (44) has proposed a model relating ac losses to hysteresis caused by surface imperfections. Moreover, it is now recognized (21) that type III superconductors may carry a (small) lossless surface current in fields up to an $H_{c3} > H_{c2}$; and that (45) such a surface current may also exist in the mixed state where $H_{c1} \leq H \leq H_{c2}$. There is increasing experimental evidence (46) that surface currents contribute to the hysteresis of type III superconductors.

II. THEORY

We assume that the dominant mechanism for the ac loss of a type III superconductor is bulk hysteresis and that the situation may be described by a critical distribution of field and current within the body. According to B. Montgomery, as reported by Riemersma (17), the distribution must be critical because magnetization measurements (in the mixed state) indicate decreasing induced current with increasing applied field, contrary to what would be expected from Faraday's law. So there must be a critical state which limits current density in the body to some value consistent with that state. Of the critical state models mentioned in Section I.D.2, we adopt the Riemersma model, i.e., Eq. (6). This is tantamount to assuming that on a macroscopic scale there is a uniform pinning force, equal and opposite to the Lorentz force, within the region of penetration, a reasonable assumption that is convenient in its simplicity.

A. The Initial Excitation

Figure 11 shows the geometry and the variables of interest. We assume that I is increased monotonically from zero in the virgin state of the material. When I exceeds $2\pi R H_{c1}$, the superconductor enters the mixed state and penetration of current density, magnetic induction, and electric field occurs to a radius ρ. Within this radius **J**, **B**, and **E** are zero. For $\rho \leq r \leq R$, **B** may be determined as follows. Assuming $\mathbf{M} = 0$ (the $\mu = \mu_0$ interpretation of the Meissner effect) and using the quasistatic approximation,

$$\text{curl } \mathbf{B} = \mu_0 \mathbf{J}, \tag{7}$$

together with Eq. (6), we have

$$B \frac{dB}{dr} + \frac{B^2}{r} = \mu_0 C. \tag{8}$$

This is a Bernoulli equation with the solution

$$B^2 = \frac{2}{3} \mu_0 Cr + \frac{k_1}{r^2} \cdot \tag{9}$$

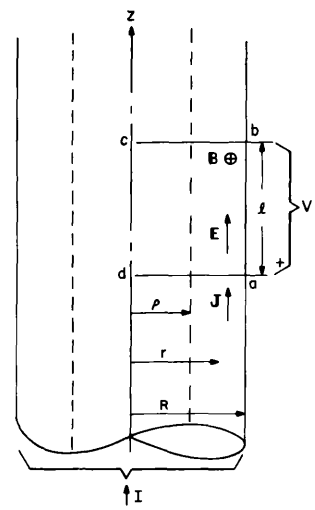

Fig. 11 – Portion of a long type-III superconductor carrying an alternating transport current (I) such that penetration of current density (J), magnetic induction (B), and electric field (E) occurs to a radius ρ, causing a surface voltage drop V

Applying the boundary condition

$$B(R) = \frac{\mu_0 I}{2\pi R}, \tag{10}$$

we find

$$\frac{B^2}{\mu_0} = \frac{2}{3} Cr + \left(\frac{\mu_0 I^2}{4\pi^2} - \frac{2}{3} CR^3 \right) \frac{1}{r^2}, \tag{11}$$

where $\rho \leq r \leq R$. To obtain the penetration radius $\rho(I)$, we use the boundary condition

$$B(\rho) = 0. \tag{12}$$

This in Eq. (11) gives

$$\rho^3 = R^3 - \frac{3\mu_0 I^2}{8\pi^2 C}, \tag{13}$$

where $2\pi RH_{c1} < I \leq I_c$ and I_c is the critical current at which penetration is complete and the body goes normal. The critical current is found by putting $\rho = 0$ in Eq. (13). Thus

$$I_c^2 = \frac{8\pi^2 CR^3}{3\mu_0}. \tag{14}$$

The single parameter of this model, the pinning force constant C, may therefore be determined experimentally by measurement of the critical current. From Eqs. (6) and (11) the current density is given by

$$J^2 = \frac{C^2}{\mu_0\left[\frac{2}{3}Cr + \left(\frac{\mu_0 I^2}{4\pi^2} - \frac{2}{3}CR^3\right)\frac{1}{r^2}\right]}, \tag{15}$$

where $\rho \leq r \leq R$. The distribution of magnetic field and current density is depicted in Fig. 12.

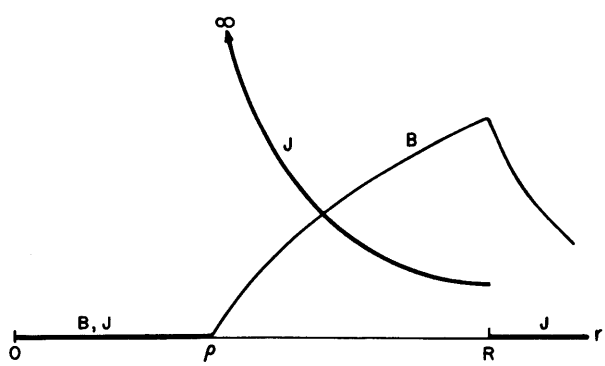

Fig. 12 – Distribution of magnetic field and current density during initial excitation of the superconductor in Fig. 11

1. **The Induced Voltage.** The induced emf in loop abcd of Fig. 11 is found from Faraday's law:

$$\oint_{abcd} \mathbf{E} \cdot d\mathbf{s} = -\dot{\varphi}, \tag{16}$$

where φ is the magnetic flux enclosed by the path of integration. But

$$\oint_{abcd} \mathbf{E} \cdot d\mathbf{s} = \int_{ab} \mathbf{E} \cdot d\mathbf{s} + \int_{bc} \mathbf{E} \cdot d\mathbf{s} + \int_{cd} \mathbf{E} \cdot d\mathbf{s} + \int_{da} \mathbf{E} \cdot d\mathbf{s}, \tag{17}$$

and

$$\int_{bc} \mathbf{E} \cdot d\mathbf{s} = \int_{cd} \mathbf{E} \cdot d\mathbf{s} = \int_{da} \mathbf{E} \cdot d\mathbf{s} = 0 \tag{18}$$

because $\mathbf{J} \cdot d\mathbf{s} = 0$ on these paths and the conductivity $\sigma \neq 0$ in

$$\mathbf{J} = \sigma \mathbf{E}. \tag{19}$$

Therefore the voltage drop along surface ab is

$$V \triangleq - \int_{ab} \mathbf{E} \cdot d\mathbf{s} = - \int_{abcd} \mathbf{E} \cdot d\mathbf{s} = \dot{\varphi}. \tag{20}$$

This result has already been used by Grasmehr (47) and Taylor (48). The flux is given by

$$\varphi = \int_{\rho}^{R} \ell \, B \, dr. \tag{21}$$

Putting Eq. (13) into Eq. (11) and Eq. (11) into Eq. (21), we have

$$\varphi(\rho) = \ell \sqrt{\frac{2}{3} \mu_0 C} \int_{\rho}^{R} \sqrt{r - \frac{\rho^3}{r^2}} \, dr. \tag{22}$$

From Eq. (20), the voltage may be expressed as

$$V = \frac{d\varphi}{d\rho} \frac{d\rho}{dI} \dot{I}. \tag{23}$$

If only the voltage is desired (in order to obtain the power) evaluation of φ may be avoided by differentiation under the integral sign (49) in Eq. (22). That gives

$$\frac{d\varphi}{d\rho} = - \ell \sqrt{\frac{2}{3} \mu_0 C} \left(R^3 - \frac{3 \mu_0 I^2}{8 \pi^2 C} \right)^{1/6} \arctan I \sqrt{\frac{3 \mu_0}{8 \pi^2 C R^3 - 3 \mu_0 I^2}} \, . \tag{24}$$

From Eq. (13) the derivative of ρ with respect to I is

$$\frac{d\rho}{dI} = -\frac{\mu_0 I}{4\pi^2 C}\left(R^3 - \frac{3\,\mu_0 I^2}{8\,\pi^2 C}\right)^{-2/3} . \tag{25}$$

Then using Eq. (14) with Eqs. (24) and (25), we have

$$V_0 = \frac{\mu_0 \ell}{3\,\pi}\,\frac{I\,\dot{I}}{\sqrt{I_c^{\,2} - I^2}}\,\arctan\frac{I}{\sqrt{I_c^{\,2} - I^2}}, \tag{26}$$

where $2\pi R H_{c1} < I \leq I_c$, and the zero subscript on V denotes initial excitation.

B. The Hysteresis Loop

We assume that I decreases monotonically from some peak value $I_m \leq I_c$ to a negative peak $-I_m$, increases again to I_m with half-wave symmetry, and is periodic thereafter.

1. **The Voltage Equations.** Four operating regimes must be considered.

Regime I: $\dot{I} < 0,\ 0 \leq I \leq I_m$

In any critical state model as I is reduced below I_m, **J** reverses at the surface, and an interface is established (at $r = \delta$) separating regions of oppositely directed **J**. The new situation is represented in Fig. 13. The penetration radius is now fixed at $\rho_m \triangleq \rho(I_m)$ given by Eq. (13). Solutions must be found in the two regions distinguished by the new variable $\delta(I)$.

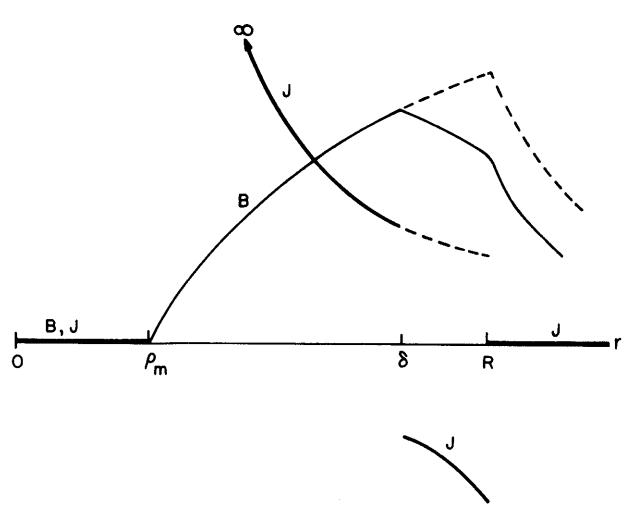

Fig. 13 – Field and current distribution in the superconductor of Fig. 11 when $\dot{I} < 0$ and $0 < I < I_m$

Region a: $\rho_m \leq r \leq \delta$

Since the new current distribution is external to this region and has azimuthal symmetry, the form of the magnetic field is unchanged. Equation (11) applies with $I = I_m$, as does Eq. (15).

Region b: $\delta \leq r \leq R$

In this region, Eq. (6) as a scalar equation is written $BJ = -C$ in order to keep C a positive constant. The direction of the Lorentz force, and therefore that of the pinning force, is reversed in the two regions separated by $r = \delta$. The solution for B in the outer region, analagous to Eq. (9), is

$$B^2 = \frac{k_2}{r^2} - \frac{2}{3}\mu_0 Cr. \tag{27}$$

Applying the boundary condition to Eq. (11) with $I = I_m$ and Eq. (27) that B is continuous at $r = \delta$, we have

$$\frac{B^2}{\mu_0} = \left[\frac{\mu_0 I_m{}^2}{4\pi^2} - \frac{2}{3}C\,(R^3 - 2\delta^3)\right]\frac{1}{r^2} - \frac{2}{3}Cr. \tag{28}$$

The new variable $\delta(I)$ is then evaluated by the boundary condition of Eq. (10). The result is

$$\delta^3 = R^3 - \frac{3\mu_0}{16\,\pi^2 C}\,(I_m{}^2 - I^2). \tag{29}$$

From Eqs. (11) with $I = I_m$ and (28) in Eq. (21), we find that the flux is

$$\phi_I = \ell\sqrt{\frac{2}{3}\,\mu_0 C}\left[\int_{\rho_m}^{\delta}\sqrt{r - \frac{\rho_m{}^3}{r^2}}\,dr + \int_{\delta}^{R}\sqrt{\frac{(2\delta^3 - \rho_m{}^3)}{r^2} - r}\,dr\right], \tag{30}$$

where we have used ρ_m from Eq. (13). The subscript I means $\dot{I} < 0$ and $0 \leq I \leq I_m$. Voltage is found from

$$V = \frac{d\varphi}{d\delta}\,\frac{d\delta}{dI}\,\dot{I} \tag{31}$$

in the same way as for Section II.A.1; the result is

$$V_I = \frac{\mu_0 \ell I \dot{I}}{3\pi\sqrt{I_c{}^2 + I^2}}\left[\arg\tanh\sqrt{\frac{I_m{}^2 + I^2}{2\,(I_c{}^2 + I^2)}} - \arg\tanh\frac{I}{\sqrt{I_c{}^2 + I^2}}\right]. \tag{32}$$

Regime II: $\dot{I} < 0, \; -I_m \leq I \leq 0$

When I reaches zero, the situation is shown in Fig. 14. The particular value of δ, say δ_r, is given by Eq. (29):

$$\delta_r^3 = \rho_m^3 + \frac{3\mu_0 I_m^2}{16\pi^2 C}, \tag{33}$$

or, using Eq. (14),

$$\delta_r^3 = \rho_m^3 + \frac{R^3 I_m^2}{2 I_c^2}. \tag{34}$$

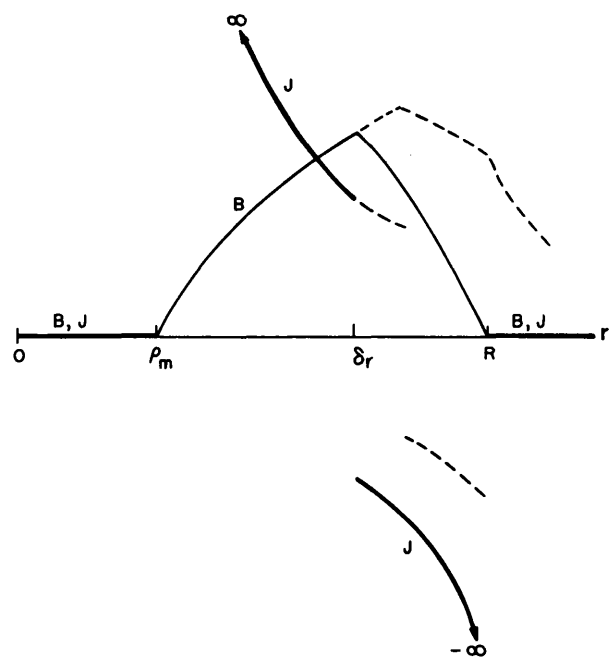

Fig. 14 – Field and current distribution in the superconductor of Fig. 11 when $\dot{I} < 0$ and $I = 0$

Further reduction of I causes the current density to again reverse at the surface, and a new interface at $r = \zeta$ begins to move inward, as shown in Fig. 15. There are now three distinct regions to be considered; an outline of the solution follows.

Region a: $\rho_m \leq r \leq \delta$

Equations (11) for B and (15) for J still apply with $I = I_m$.

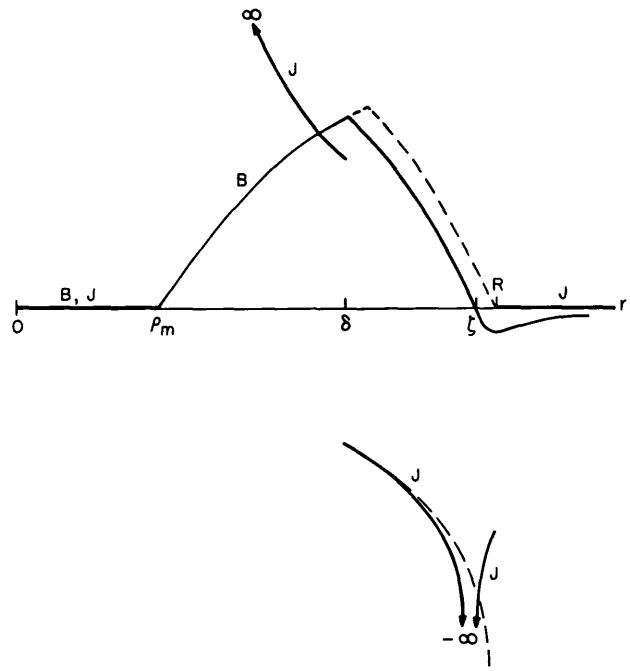

Fig. 15 – Field and current distribution in the superconductor of Fig. 11 when $\dot{I} < 0$ and $I < 0$

Region b: $\delta \leq r \leq \zeta$

Equation (27) still applies, so Eq. (28) may be used for B in this region, but δ is no longer given by Eq. (29) because of a new boundary condition.

Region c: $\zeta \leq r \leq R$

Since both B and $J < 0$, $BJ = C$, as in Case I, and the boundary condition of Eq. (10) also holds here, B is given by Eq. (11) in this region.

The new variable $\zeta(I)$ may be evaluated by the boundary condition that $B = 0$ in Eq. (11) at $r = \zeta$. This gives

$$\zeta^3 = R^3 \left(1 - \frac{I^2}{I_c^2}\right). \tag{35}$$

An expression for $\delta(I)$ is found by the same condition imposed on Eq. (28):

$$\delta^3 = R^3 \left[1 - \frac{(I_m^2 + I^2)}{2I_c^2}\right]. \tag{36}$$

The flux for Regime II is

$$\varphi_{II} = \ell \sqrt{\frac{2}{3}\mu_0 C} \left\{ \int_{\rho_m}^{\delta} \sqrt{r - (I_c^2 - I_m^2)\frac{R^3}{I_c^2 r^2}}\, dr \right.$$

$$+ \int_{\delta}^{\zeta} \sqrt{\left[2\delta^3 - (I_c^2 - I_m^2)\frac{R^3}{I_c^2}\right]\frac{1}{r^2} - r}\, dr$$

$$\left. + \int_{\zeta}^{R} \sqrt{r - (I_c^2 - I^2)\frac{R^3}{I_c^2 r^2}}\, dr \right\}, \tag{37}$$

and the voltage is

$$V_{II} = \frac{\mu_0 \ell I \dot{I}}{3\pi\sqrt{I_c^2 - I^2}} \left[\arctan \frac{I}{\sqrt{I_c^2 - I^2}} - \arg\tanh \sqrt{\frac{I_m^2 - I^2}{2(I_c^2 - I^2)}} \right]. \tag{38}$$

Regime III: $\dot{I} > 0$, $-I_m \geq I \geq 0$

Inasmuch as the current waveform was assumed to possess half-wave symmetry, and it can be shown from Eq. (37) that $\varphi_{II}(-I_m) = -\varphi_I(I_m)$, the φ-I hysteresis loop will be symmetrical as indicated in Fig. 16. It follows, therefore, that the voltage waveform will also possess half-wave symmetry. Consequently the voltage for Regime III may be written by inspection of V_I:

$$V_{III} = -\frac{\mu_0 \ell I \dot{I}}{3\pi\sqrt{I_c^2 + I^2}} \left[\arg\tanh \sqrt{\frac{I_m^2 + I^2}{2(I_c^2 + I^2)}} + \arg\tanh \frac{I}{\sqrt{I_c^2 + I^2}} \right]. \tag{39}$$

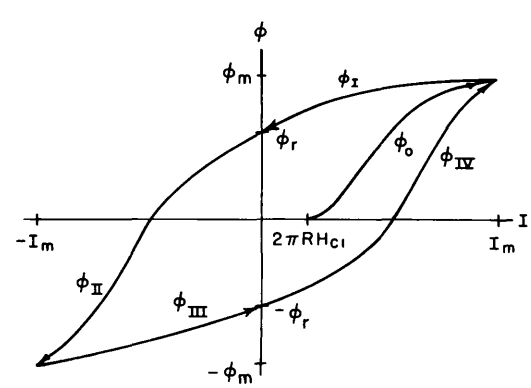

Fig. 16 – Initial excitation curve and major hysteresis loop in the φ – I plane for the superconductor of Fig. 11

Regime IV: $\dot{I} > 0$, $0 \leq I \leq I_m$

Similarly the voltage for Regime IV may be written by inspection of V_{II}:

$$V_{IV} = \frac{\mu_0 \ell I \dot{I}}{3\pi \sqrt{I_c^2 - I^2}} \left[\arctan \frac{I}{\sqrt{I_c^2 - I^2}} + \arg \tanh \sqrt{\frac{I_m^2 - I^2}{2(I_c^2 - I^2)}} \right]. \tag{40}$$

Theoretical voltage waveforms for a half cycle of sinusoidal and triangular current are shown in Figs. 17 and 18, respectively, for various ratios of I_c/I_m. The volt-ampere characteristic with a sinusoidal current is shown in Fig. 19.

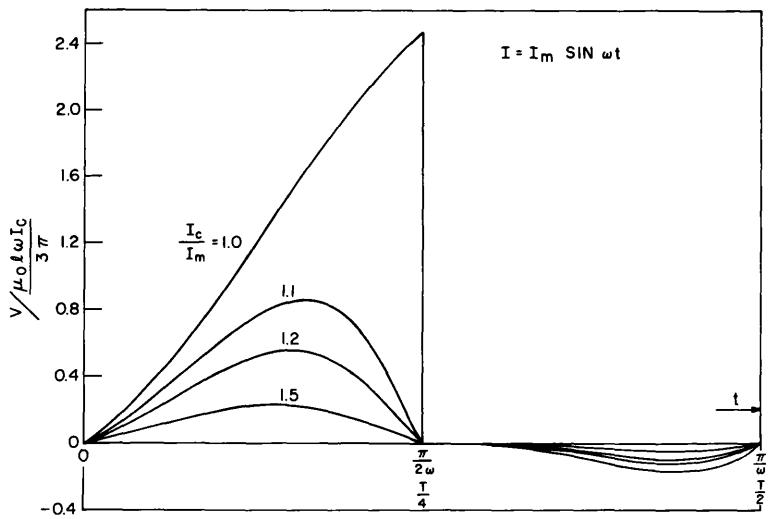

Fig. 17 – Predicted voltage waveforms for a half cycle of sinusoidal current having various ratios of I_c/I_m in a type III superconductor

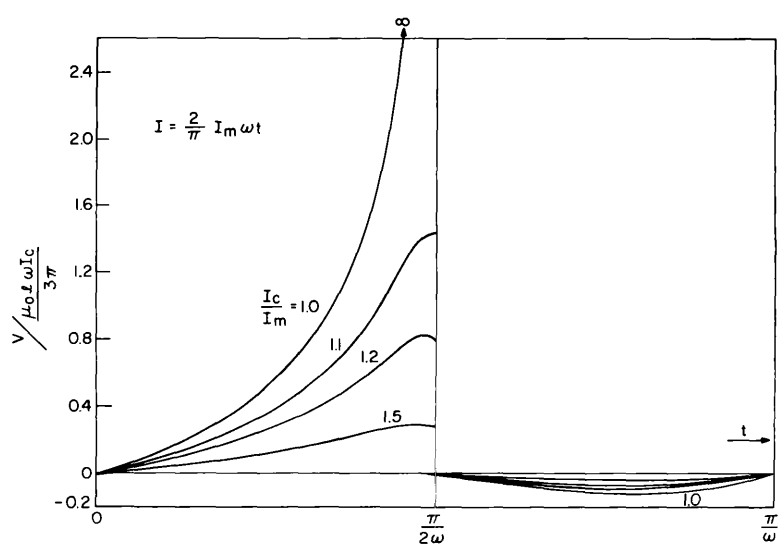

Fig. 18 – Predicted voltage waveforms for a half cycle of triangular current having various ratios of I_c/I_m in a type III superconductor

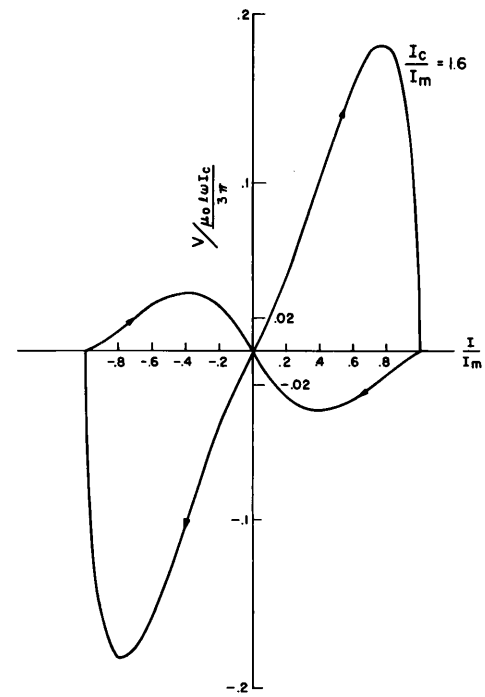

Fig. 19 – Predicted volt-amp characteristic for a sinusoidal current of a particular I_c/I_m ratio in a type III superconductor

2. **The Loss per Cycle.** For an alternating current of period T, the energy loss per cycle is

$$\epsilon = \int_{t_1}^{t_1+T} V\, I\, dt. \tag{41}$$

Since both voltage and current have half-wave symmetry,

$$\epsilon = 2 \int_{t_1}^{t_1+T/2} V\, I\, dt, \tag{44}$$

so that only V_I and V_{II} need be considered. Because both are proportional to $\dot{I}$, the loss is

$$\epsilon = \frac{2\mu_0 \ell}{3\pi} \left\{ \int_{I_m}^{0} \left[\text{arg tanh} \sqrt{\frac{I_m^2 + I^2}{2(I_c^2 + I^2)}} - \text{arg tanh} \frac{I}{\sqrt{I_c^2 + I^2}} \right] \frac{I^2\, dI}{\sqrt{I_c^2 + I^2}} \right.$$
$$\left. + \int_{0}^{-I_m} \left[\arctan \frac{I}{\sqrt{I_c^2 - I^2}} - \text{arg tanh} \sqrt{\frac{I_m^2 - I^2}{2(I_c^2 - I^2)}} \right] \frac{I^2\, dI}{\sqrt{I_c^2 - I^2}} \right\}. \tag{45}$$

By sorting out even and odd functions the terms can be combined under a single integral sign. Defining the quantities $x \triangleq I/I_c$ and $y \triangleq I_m/I_c$ results in the relatively simple expression

$$\epsilon = \frac{2\mu_0 \ell}{3\pi} I_c^2 \int_0^y \left[\frac{\arcsin x + \arg\tanh \sqrt{\frac{y^2 - x^2}{2(1 - x^2)}}}{\sqrt{1 - x^2}} + \frac{\arg\sinh x - \arg\tanh \sqrt{\frac{y^2 + x^2}{2(1 + x^2)}}}{\sqrt{1 + x^2}} \right] x^2 \, dx. \tag{46}$$

It is clear that Eq. (46) gives a loss per cycle that is independent of current waveform and frequency; it depends only on the amplitude of the current. Equation (46) was numerically integrated on a digital computer. The result is shown in Fig. 20 for a range of y. The behavior of Eq. (46) for extreme values of y is discussed in Appendix A. The average power loss is

$$\bar{p} \triangleq \frac{\epsilon}{T} \triangleq \epsilon f, \tag{47}$$

where T is the period and f the frequency. The power loss is thus a linear function of the frequency as expected for hysteresis.

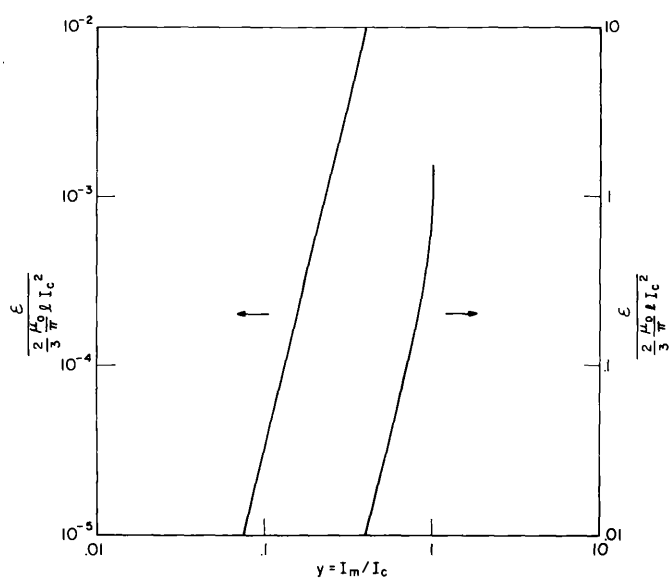

Fig. 20 – Predicted hysteresis loss per cycle for a type III superconductor

3. **The Effective Resistivity.** Appendix A shows that for small currents the energy loss per cycle is

$$\epsilon = 0.912 \times 10^{-7} \frac{I_m^4}{I_c^2} \ell \text{ joule.} \tag{48}$$

Defining an effective resistance by $\bar{p} \triangleq R_e I_{rms}^2$ and assuming a sinusoidal current (for which the peak factor is $I_m/I_{rms} = \sqrt{2}$),

$$R_e = 3.67 \times 10^{-7} \ell f \left(\frac{I_{rms}}{I_c}\right)^2 \text{ ohm.} \tag{49}$$

The resistivity ρ is defined by

$$R_e = \rho \frac{\ell}{a} \tag{50}$$

where a is the cross-sectional area. For 10-mil wire

$$a = 5.06 \times 10^{-8} \text{ m}^2, \tag{51}$$

and

$$\rho = 1.86 \times 10^{-14} f \left(\frac{I_{rms}}{I_c}\right)^2 \text{ ohm-meter.} \tag{52}$$

For the maximum superconducting current, i.e., $I_m = I_c$, Appendix A gives an energy loss per cycle of

$$\epsilon = 4.01 \times 10^{-7} \ell I_c^2 \text{ joule.} \tag{53}$$

Again assuming a sinusoidal current,

$$R_e = 8.02 \times 10^{-7} \ell f \text{ ohm,} \tag{54}$$

and for 10-mil wire

$$\rho = 4.06 \times 10^{-14} f \text{ ohm-meter.} \tag{56}$$

Note that Eq. (56) and, for a given I_m/I_c ratio, Eq. (52) are independent of the particular material involved.

C. An Equivalent Circuit

The effective resistivity derived above may be used as the basis of an equivalent circuit for a type III superconductor. Such a circuit, consisting of a simple resistor,

would give, by definition, the average steady-state power loss for a sinusoidal current; however it could not give the instantaneous behavior of the superconductor.

A more realistic equivalent circuit is obtained by treating the superconductor as an inductor having a variable self inductance. The variation of inductance is due to penetration in the mixed state, which causes changes in the field and current distributions. Since the external field for a given current is independent of the current distribution, we may focus our attention on the "internal inductance" representing flux internal to the superconductor. We recall that many electric machines operate, from a circuit point of view, by time-variation of a parameter (50). We may think of a hysteretic superconductor as a parametric motor where work is done to move fluxoids through a viscous medium. The ordinary parametric machine is a linear device in that it may be described by linear differential equations with time-varying coefficients. The type III superconductor, however, is nonlinear. As we shall see, the internal inductance is a function of current; moreover, the function is different for different ranges of the current and its first derivative.

Because of the nonlinearity, various definitions of inductance may be adopted, each of which is reasonable in itself. Appendix B discusses three kinds of inductance and shows them to be nonequivalent in our case. The definition we prefer is the so-called absolute inductance (51):

$$L_a \triangleq \frac{\psi}{I}, \tag{57}$$

where ψ denotes flux linkages. A summary of equations for this inductance, as well as for the induced voltage, is presented in Table 1. The absolute inductance is not the most convenient analytically, but it has the advantage of being directly related to the flux which penetrates the superconductor. For example, multiplication of the inductance in Table 1 by I and passage to the limit of I = 0 gives the so-called trapped flux.

The maximum value of the absolute internal inductance occurs at the critical current and is

$$\lim_{I \to I_c} L_a = \frac{\mu_0 \ell}{3\pi}. \tag{58}$$

This may be compared with the internal inductance of an infinite, normal conductor (52):

$$L_i = \frac{\mu_0 \ell}{8\pi}. \tag{59}$$

It is ironic that the type III superconductor, which is "diamagnetic" and attempts to exclude flux, ultimately permits more flux linkages per ampere than a normal conductor. A formal explanation for this is offered in Appendix B.

Table 1

Absolute Internal Inductances and Induced Voltages

Regime	L_a	V
$2\pi R H_{c1} < I \le I_c$, $\dot{I} > 0$	$\frac{\mu_0 \ell}{3\pi}\left[1 - \frac{\sqrt{I_c^2 - I^2}}{I}\arctan\frac{I}{\sqrt{I_c^2 - I^2}}\right]$	$\frac{\mu_0 \ell}{3\pi}\frac{I\dot{I}}{\sqrt{I_c^2 - I^2}}\arctan\frac{I}{\sqrt{I_c^2 - I^2}}$
$0 \le I \le I_m \le I_c$, $\dot{I} < 0$	$\frac{\mu_0 \ell}{3\pi}\left\{1 - \frac{\sqrt{I_c^2 - I_m^2}}{I}\arctan\sqrt{\frac{I_m^2 + I^2}{2(I_c^2 - I_m^2)}} + \frac{\sqrt{I_c^2 + I^2}}{I}\left[\operatorname{arg\,tanh}\sqrt{\frac{I_m^2 + I^2}{2(I_c^2 + I^2)}} - \operatorname{arg\,tanh}\frac{I}{\sqrt{I_c^2 + I^2}}\right]\right\}$	$\frac{\mu_0 \ell I \dot{I}}{3\pi\sqrt{I_c^2 + I^2}}\left[\operatorname{arg\,tanh}\sqrt{\frac{I_m^2 + I^2}{2(I_c^2 + I^2)}} - \operatorname{arg\,tanh}\frac{I}{\sqrt{I_c^2 + I^2}}\right]$
$-I_m \le I \le 0$, $\dot{I} < 0$	$\frac{\mu_0 \ell}{3\pi}\left\{1 - \frac{\sqrt{I_c^2 - I_m^2}}{I}\arctan\sqrt{\frac{I_m^2 - I^2}{2(I_c^2 - I_m^2)}} + \frac{\sqrt{I_c^2 - I^2}}{I}\left[\operatorname{arg\,tanh}\sqrt{\frac{I_m^2 - I^2}{2(I_c^2 - I^2)}} - \arctan\frac{I}{\sqrt{I_c^2 - I^2}}\right]\right\}$	$\frac{\mu_0 \ell I \dot{I}}{3\pi\sqrt{I_c^2 - I^2}}\left[\arctan\frac{I}{\sqrt{I_c^2 - I^2}} - \operatorname{arg\,tanh}\sqrt{\frac{I_m^2 - I^2}{2(I_c^2 - I^2)}}\right]$
$-I_m \le I \le 0$, $\dot{I} > 0$	$\frac{\mu_0 \ell}{3\pi}\left\{1 + \frac{\sqrt{I_c^2 - I_m^2}}{I}\arctan\sqrt{\frac{I_m^2 + I^2}{2(I_c^2 - I_m^2)}} - \frac{\sqrt{I_c^2 + I^2}}{I}\left[\operatorname{arg\,tanh}\sqrt{\frac{I_m^2 + I^2}{2(I_c^2 + I^2)}} + \operatorname{arg\,tanh}\frac{I}{\sqrt{I_c^2 + I^2}}\right]\right\}$	$\frac{-\mu_0 \ell I \dot{I}}{3\pi\sqrt{I_c^2 + I^2}}\left[\operatorname{arg\,tanh}\sqrt{\frac{I_m^2 + I^2}{2(I_c^2 + I^2)}} + \operatorname{arg\,tanh}\frac{I}{\sqrt{I_c^2 + I^2}}\right]$
$0 \le I \le I_m$, $\dot{I} > 0$	$\frac{\mu_0 \ell}{3\pi}\left\{1 + \frac{\sqrt{I_c^2 - I_m^2}}{I}\arctan\sqrt{\frac{I_m^2 - I^2}{2(I_c^2 - I_m^2)}} - \frac{\sqrt{I_c^2 - I^2}}{I}\left[\operatorname{arg\,tanh}\sqrt{\frac{I_m^2 - I^2}{2(I_c^2 - I^2)}} + \arctan\frac{I}{\sqrt{I_c^2 - I^2}}\right]\right\}$	$\frac{\mu_0 \ell I \dot{I}}{3\pi\sqrt{I_c^2 - I^2}}\left[\arctan\frac{I}{\sqrt{I_c^2 - I^2}} + \operatorname{arg\,tanh}\sqrt{\frac{I_m^2 - I^2}{2(I_c^2 - I^2)}}\right]$

III. THE EXPERIMENT

The ac losses of type III superconductors have been measured by calorimetry (16, 53-65) and by electrical methods (15, 44, 66-75). There have been measurements on wires of different types, in different sizes, in various configurations and windings, and subjected to a variety of conditions. We used an electrical method that no one else seems to have used. Current and (compensated) voltage waveforms were obtained and their product integrated by computer.

A. The Specimens

A considerable length of wire was desired in order to enjoy a good signal-to-noise ratio. On the other hand, a simple configuration was desired for comparison with a tractable model. A bifilar winding was used to simulate an infinite line that could be analyzed by the theory of Section II. Two specimens of 10-mil, Nb-25%Zr wire were prepared: one bare, the other plated with 1 mil of copper and insulated with 0.5 mil of Epoxy, both from the Kawecki Chemical Company. The wire was wound on a threaded former of glass cloth-inserted phenolic (2-1/2 in. in diameter, 8 in. long) as a single-layer bifilar winding with a 1/8-in. spacing between turns. One specimen with current and voltage leads is shown in Fig. 21.

It is important to obtain good contacts between the superconducting wire and the external circuit in order to minimize heating at the junctions. Current leads were of copper and were soldered inside two 4-in. lengths of 3/8-in. copper tubing that projected 3 in. from one end of the former. The tubing was threaded to receive the specimen wire, and the ends of the copper-clad sample were soldered to the tubing. Ends of the bare-wire sample were first copper plated and then soldered to the tubing. Voltage connections were made to the specimen between the tubing and the former so as to be within the superconducting portion of the wire sample.

It is important to minimize magnetic coupling of the specimen with external circuits. Eddy current loss in any coupled conductor would appear as a loss in the superconductor. This is another reason for using a bifilar winding. The active length of winding was approximately 12.5 m, and the self inductance measured about 7 μH. Appendix C gives a

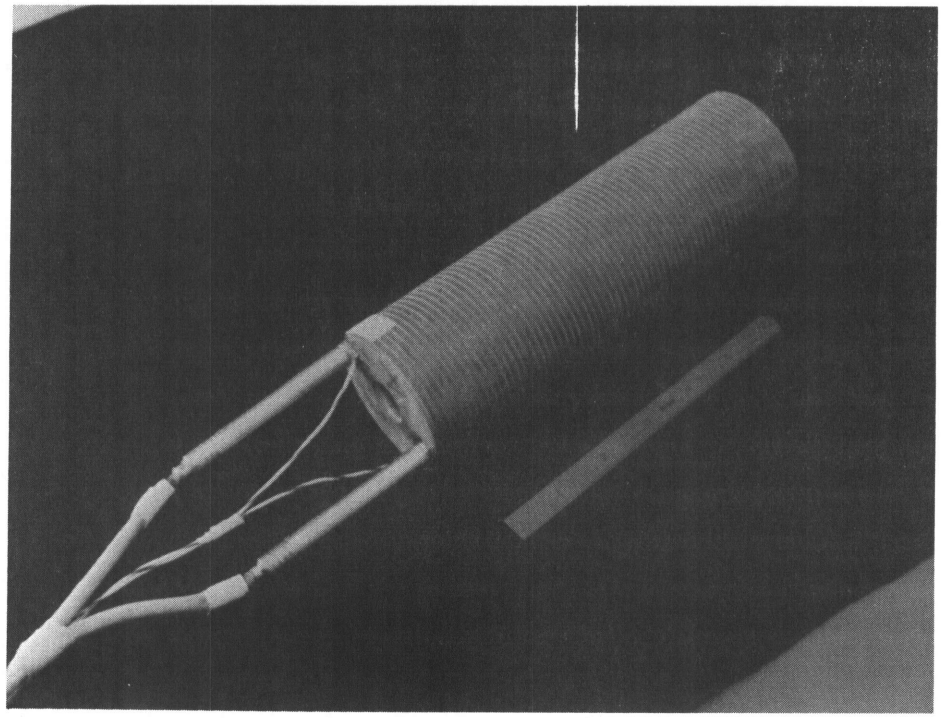

Fig. 21 – A specimen with current and voltage leads

calculation of the specimen inductance along with some measured values. Another precaution taken to minimize external coupling was removal of the silver plating in both dewars. The specimen is shown within the dewars in Fig. 22.

B. The Circuit

1. **The Compensation Method.** Even with a bifilar winding the voltage representing flux penetration (V in Section II and Fig. 11) was expected to be a small fraction of the voltage across the specimen. At low current ($I < 2\pi RH_{c1}$) the voltage V should be zero so a now standard compensation technique (44) can be used to null the undesired voltage. For this purpose others have used a fixed mutual inductor with a voltage divider to obtain the compensating voltage, but we used the variable inductor shown in Fig. 23. It is a General Radio Type 107M of which only the original rotor was used; two turns of heavy wire served as a stator. Good data were not obtained until this inductor was well removed from the rest of the circuit.

Insofar as the losses are hysteretic, the penetration voltage V may be attributed to a variable, internal (absolute) inductance L_a. The remainder of the voltage, due to distributed capacitance and the inductance of the measurement loop, is attributed to a net

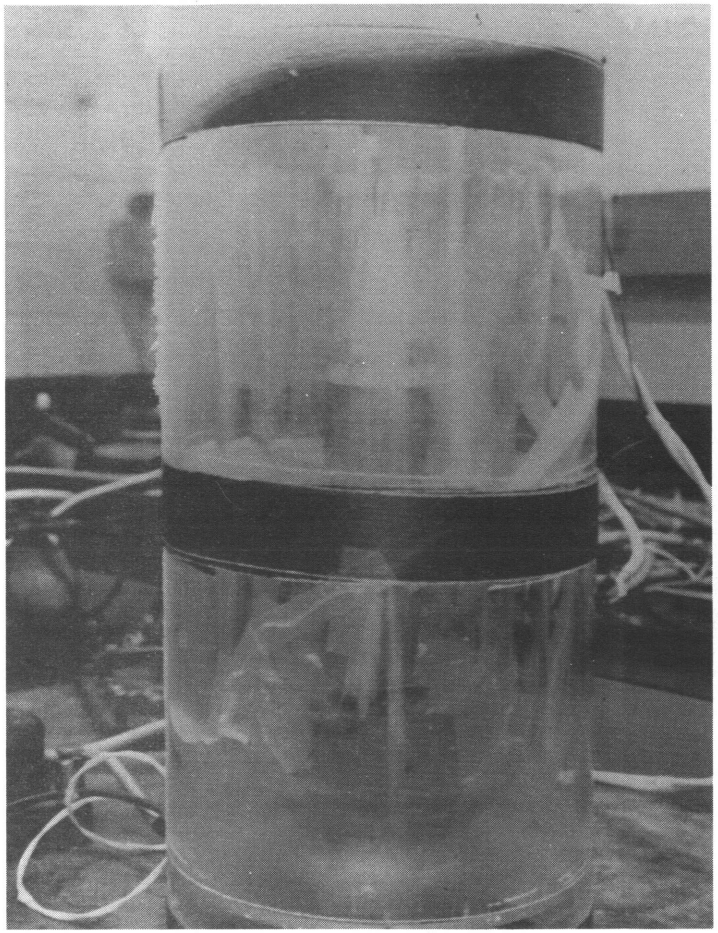

Fig. 22 – A specimen undergoing test

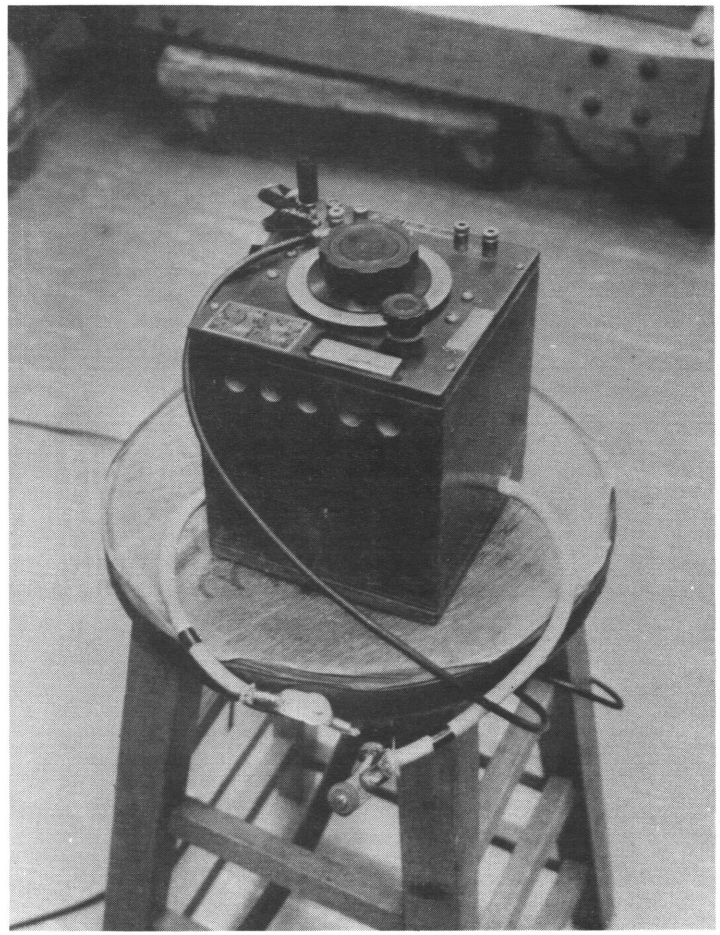

Fig. 23 – Variable inductor used for compensation

inductance L_0 which is constant at a particular frequency. This is shown in Fig. 24, from which the specimen voltage is

$$V_s = \frac{d}{dt}(L_s I). \tag{60}$$

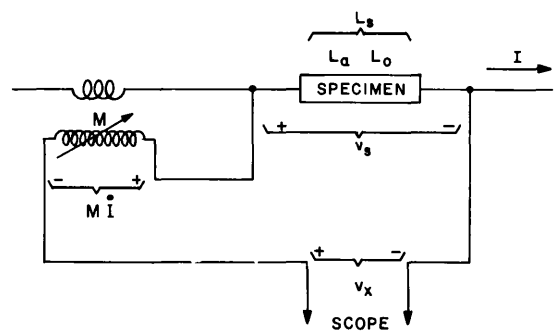

Fig. 24 – Use of a variable mutual inductor to nullify the undesired portion of the specimen voltage. The specimen has an apparent inductance L_s, of which L_a is due to internal magnetic flux and L_0 is the remainder

In terms of the above inductances,

$$V_s = \frac{d}{dt}(L_a I) + \frac{d}{dt}(L_0 I) \tag{61}$$

or, by definition,

$$V_s = V + L_0 \dot{I}. \tag{62}$$

The experimental voltage recorded is

$$V_x = V_s - M\dot{I} \tag{63}$$

$$= V + (L_0 - M)\dot{I}. \tag{64}$$

If the mutual is adjusted to null V_x at $I < 2\pi R H_{c1}$, then $M = L_0$ and for all higher currents at the same frequency

$$V_x = V. \tag{65}$$

It should be noted that this argument does not depend on a purely hysteretic loss, only on a negligible surface voltage at sufficiently low current and a constant external inductance. Thus the compensation technique is still valid if a portion of the ac loss is due to eddy currents as described in Section I. It should also be noted that the same null adjustment may be used over a wide frequency range, e.g., for nonsinusoidal currents, if distributed capacitance is negligible and the measurement loop does not couple with lossy circuits.

2. **Instrumentation.** Others (48, 66, 73, 74) have implied that the "energy loss per cycle" may be "computed by numerical integration of V-versus-I curves." This sounds plausible because it suggests an analogy with the B-H curve of ferromagnetism. But such a simple procedure is not possible; in the V-I case integration must be with respect to time, and the time dependence of the variables is not explicit in a V-I curve. It is possible to assume a current waveform, construct the voltage waveform from the V-I characteristic, plot the time variation of the VI product, and *then* integrate. We conclude that this was the procedure used in the above references.

A V-I characteristic may be obtained as a Lissajous pattern on an x-y oscilloscope. We wished to record such patterns, but at the same time desired voltage and current waveforms. Having a four-trace preamplifier plug-in unit (Tektronix Type M) and a two-operational-amplifier plug-in unit (Tektronix type O), we also observed waveforms for $\dot{I}$ and $\int V\,dt$. However, simultaneous measurement of both V and I waveforms presented the following problem. The x-y oscilloscope used for Lissajous patterns has + and − inputs to the vertical and horizontal plates, so that the V and I signals can be isolated. On the other hand, all signals into the four-channel oscilloscope have to be with respect to a common point. If the common point is put at the shunt, the voltage signal includes the IR drop in both one current lead and an indefinite length of junction; if it is at the specimen, the current signal involves the inductance of one current lead and the resistance of an indefinite length of junction. This problem was initially overcome by feeding the voltage signal from the specimen to a differential amplifier plug-in unit (Tektronix Type 53/54D) to isolate it from the current signal obtained from a calibrated shunt. In the final form of the experiment, one of the operational amplifiers was used as a differential amplifier, forgoing the luxury of an $\dot{I}$ trace. This gave a less cluttered picture of waveforms – the $\dot{I}$ trace was not used anyway – and somewhat more gain for the voltage signal. The final circuit is shown in Fig. 25; some of the experimental arrangement is shown in Figs. 26 and 27.

C. Procedure

In addition to the local source of 60 Hz, there were available 400-Hz and 800-Hz generators. There was an initial difficulty in obtaining a sinusoidal current from these sources, and this was one reason for preferring a V- and I-waveform method to the V-I characteristic method. In preliminary tests it was deemed important to have a clean current waveform so that any distortion of the voltage would be due only to superconducting phenomena. To this end a 5-kVA CML electronic generator was used for a time.

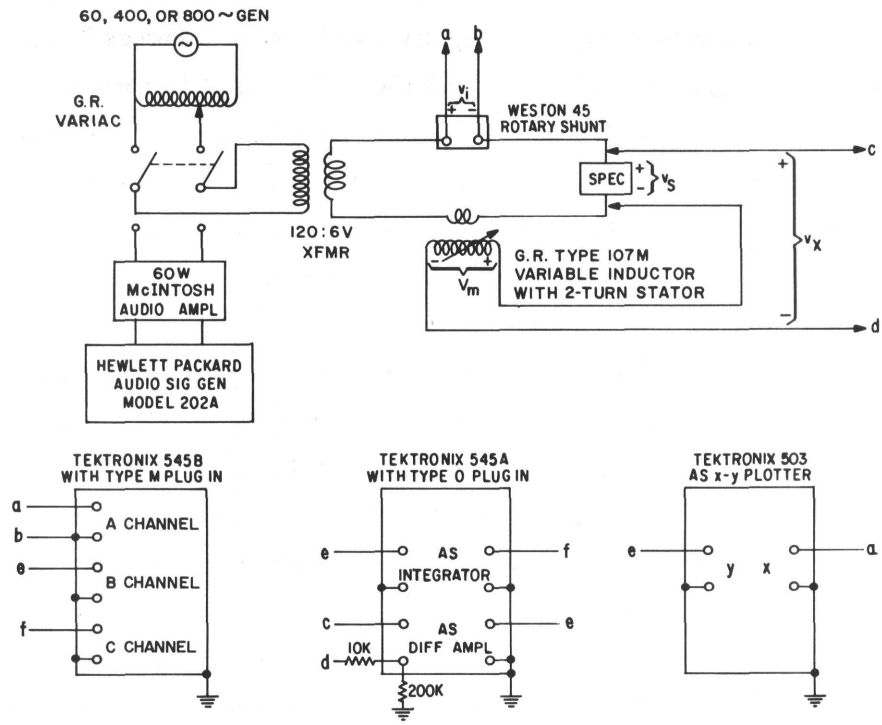

Fig. 25 – Circuit diagram of the experimental arrangement

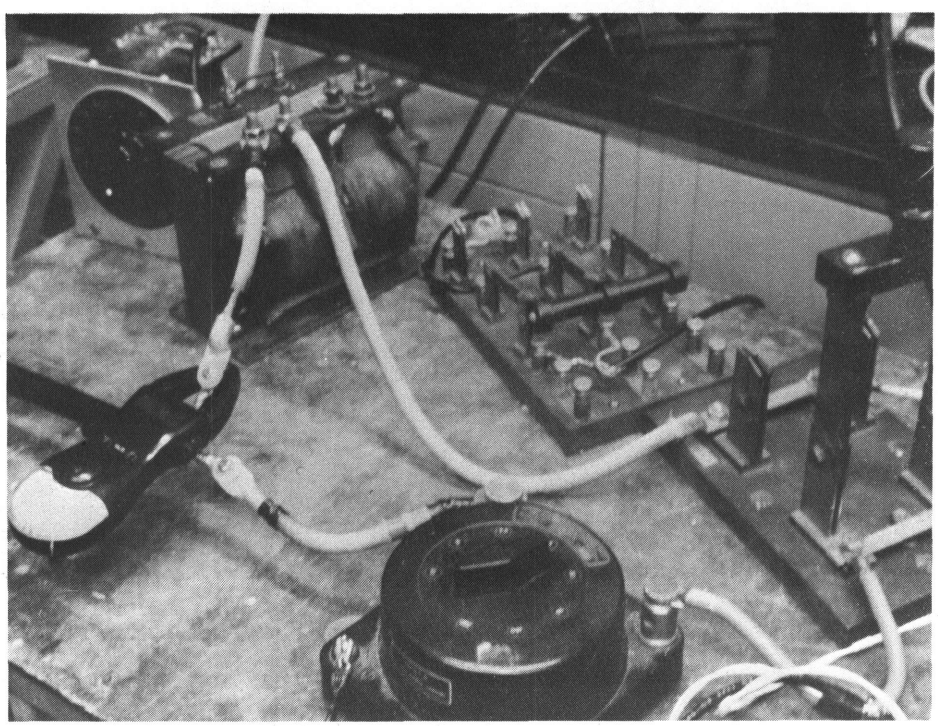

Fig. 26 – View of Variac, 120:6-V transformer, clamp-on ammeter, shunt, and switches

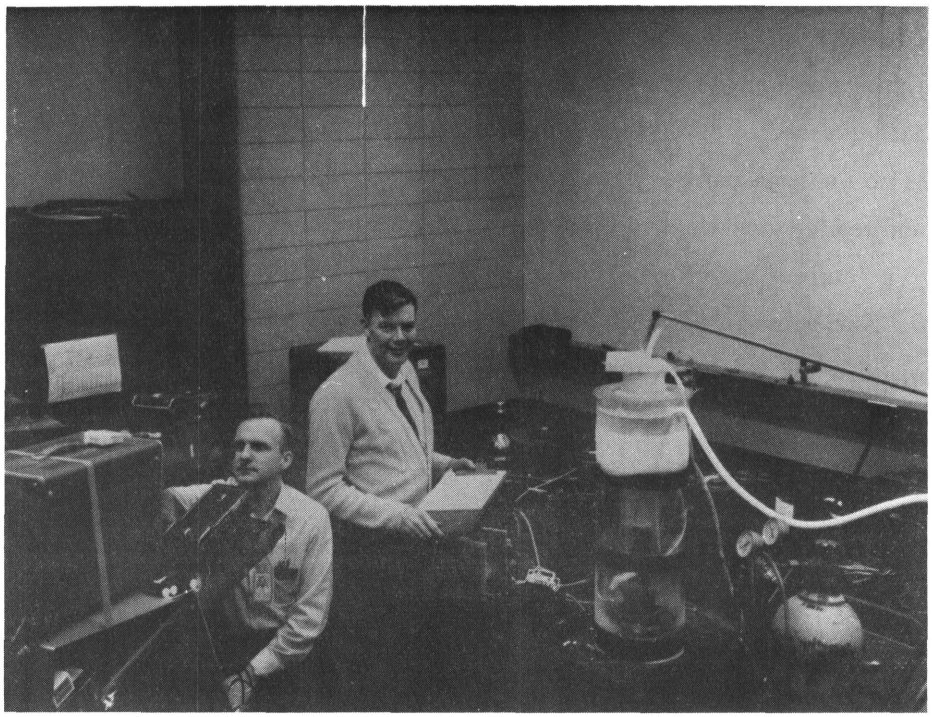

Fig. 27 – A general view of the experimental arrangement

In the final form of the experiment this was replaced by a 60-W McIntosh amplifier for low currents, especially for the null, and the first-mentioned sources for higher currents.

The dc critical current was usually measured at the beginning and end of each day's measurements. This assured a sound specimen to begin with and was supposed to detect any damage done in the course of the experiment. The null was obtained at about 0.5 amp at one of the frequencies to be used, and the setting of the mutual inductor was not changed thereafter. The null was sometimes checked on the final frequency at the end of the day's experiment. The current at each frequency was increased until a significant voltage appeared; photographs of the waveform and Lissajous displays were made there and about every 5 amperes thereafter. To save time – and liquid helium – the current was set only roughly, according to a clamp-on ammeter. Calibration of the shunt and oscilloscopes was relied upon for determination of the actual values. Current was increased at each frequency until the specimen went normal.

We attempted to begin each run at a particular frequency in the virgin state of the material and used progressively increasing excitations to avoid initial trapped flux and minor hysteresis loops. In this respect, the procedure was similar to that for measurement of a magnetization curve.

1. **Reduction of Data.** The raw data consisted of Polaroid photographs of the oscilloscope displays of V, I, and $\int V\,dt$ waveforms and of V-I characteristics. These were enlarged and reversed to give black-on-white prints for analysis. Voltage waveform data were read into punched cards by means of a Benson-Lehner Model K OSCAR (oscillograph analyzer and reader) and were referenced to the current waveforms by a phase angle measurement. The current waveforms finally obtained were of sufficient quality to be assumed sinusoidal. Numerical integration of the VI product was carried out on a Control Data Corporation 3800 digital computer with a routine based on Simpson's rule. Manual analysis and hand calculations were carried out in four cases, using a planimeter for integration, and agreement with computer results was within 3 percent.

D. Discussion of Results

1. **Waveforms.** Figure 28 shows experimental waveforms of I, V, and $\int V\,dt$ for the plated wire at 800 Hz and I_m = 76.7 A. Waveforms for the bare wire have the same appearance. The solid sinusoid is the shunt voltage trace. Because of shunt inductance, the current lags the shunt voltage as indicated by the dotted sinusoid.

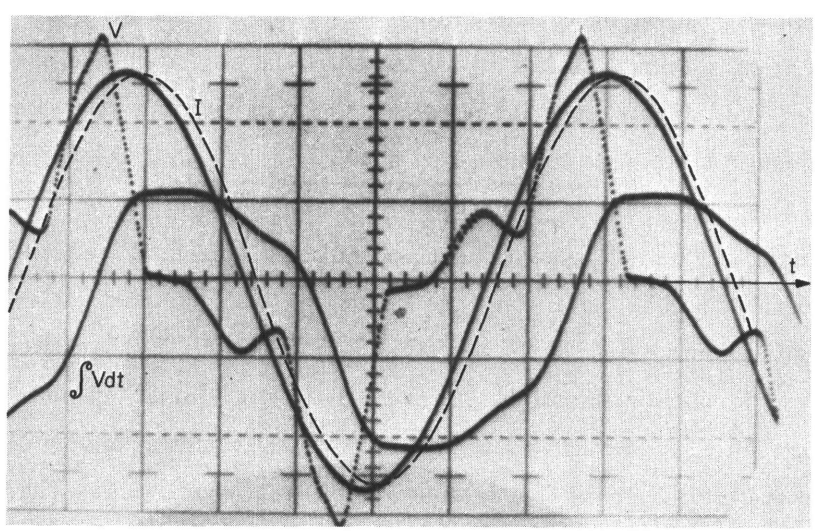

Fig. 28 – Experimental waveforms of I, V, and $\int V\,dt$ for the plated wire at 800 Hz and I_m = 76.7 A. The voltage scale is 50 mV/cm

According to Eq. (20),

$$\int V \, dt = \varphi; \tag{66}$$

so the magnetic flux waveform is given by the voltage integral. In light of the critical state model of Section II, Fig. 28 shows a reasonable variation of flux with respect to current. In particular, it displays the flux trapped at zero current.

The voltage waveform in Fig. 28 is similar to some published by Buchhold (44) and Grasmehr (47) in two different kinds of experiment. Grasmehr was unable to explain the "double-peaked voltage response," but it is a result of the theory presented here. This may be seen by extending Fig. 17 to a full cycle. The theory of Section II predicts voltage zeros at both peaks and zeros of current. Figure 28 shows voltage zeros very close to current peaks but only a local minimum near a current zero. This discrepancy is probably due to an imperfect null, which would not influence the calculated loss but which could contribute a voltage component in quadrature-leading the current.

Figure 29 shows the experimental volt-amp characteristic of the plated wire at 800 Hz and I_m = 76.6 A. The figure should be modified slightly by the shunt phase angle. Lissajous patterns for the bare wire have the same appearance. Figure 29 is in qualitative agreement with the theoretical Fig. 19 as indicated by the dotted lines of Fig. 29

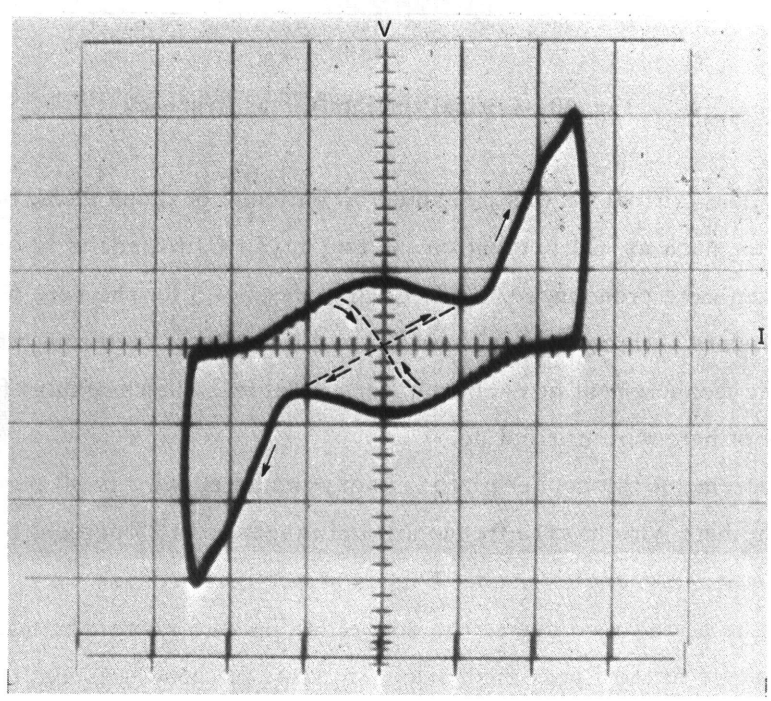

Fig. 29 – Experimental volt-amp characteristic of the plated wire at 800 Hz and I_m = 76.7 A. The voltage scale is 50 mV/cm

which might have been obtained with a perfect null. Another discrepancy, apparent in both Figs. 28 and 29 is the interval of nearly zero voltage as the current begins to descend from a positive peak or ascend from a negative peak. Flux tends to remain constant for some time thereafter. This is probably due to a surface hysteresis (76) which is not incorporated in the theory of Section II.

2. Critical Current. The variation of critical current with frequency is shown in Fig. 30. Two sets of data (15 April and 19 April) give a measure of repeatability for

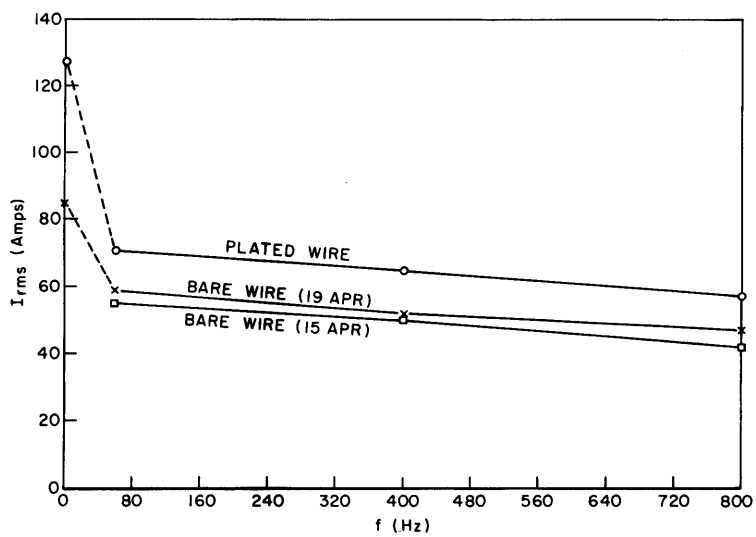

Fig. 30 – Critical currents versus frequency

the bare wire. The critical dc was measured on only one of those days, but the critical ac differed by as much as ±11 percent on the two days. (Differences in the bare wire losses were even more pronounced.) The critical dc shown for the bare wire is the result of six measurements – three each with different directions of current – whereas there was only one ac measurement at each frequency. Table 2 shows results for all the measurements made of bare-wire critical dc.

Critical current for the copper-plated, Epoxy-insulated wire is 50 percent higher than that for the bare wire at zero frequency and ranges from 25 percent to 28 percent higher for the other frequencies used. This is surprising, because we expected more dissipation in the plated wire due to the copper, along with poorer thermal conductivity to the bath because of the Epoxy insulation. In spite of these reasons, the plated wire critical current may be higher because of different metallurgical conditions in the two wires, even though they are nominally the same.

Table 2

Bare Wire Critical DC Measurements

Date	Polarity	I_c(A)
12 Feb.	+	>100
"	+	85.0
"	+	87.5
27 Feb.	+	89.0
"	+	87.2
"	+	81.9
1 Mar.	+	85.8
"	+	90.0
"	+	89.0
19 Apr.	+	85+
"	+	85.1
"	+	85.1
"	−	82.0
"	−	84.7
"	−	85.0

We know of only one published work presenting critical current data for copper plated wire. That is by Fietz *et al.* (43) and shows higher critical (direct) current densities vs applied field for a copper-plated specimen than for an Epoxy-insulated specimen, the specimens being identical, bifilar-wound coils of 10-mil, Nb-25%Zr wire. Extrapolation of these curves to the self-field case gives an even greater disparity than we observed for the critical dc. The comparison should be valid for the dc case even though their "plated wire" is not otherwise insulated and their "bare wire" is Epoxy insulated. Thomas (65) reports the reasonable result that the critical ac is less for insulated wire than for bare wire, the difference disappearing as frequency is reduced. But insofar as current was increased slowly enough in the Fietz experiment, the temperature gradient across the Epoxy from transient dissipation was negligible. If so, and if the effect in both instances (Fietz's and ours) is not due to metallurgical differences, copper must be playing some unknown role in the situation. There has been a proximity effect noticed with copper-plating—reduction of the superconducting surface sheath (77)—but that would work in the wrong direction to explain these results.

According to Fig. 30, critical currents fall off with increasing frequency as reported by some others (57, 58, 73, 78). There is a considerable range of values reported for 10-mil, Nb-25%Zr wire, even for straight-wire samples. Our highest bare wire critical current at 60 Hz is 59 A, compared to 101 A for Young and Schenk, and 107.5 A for Taylor, all in rms values. Our low value may be due to the fact that the material in these three cases came from different suppliers. Rogers (79) reports rms critical currents of 42 A and 95 A at 50 Hz for short samples (8 cm) of 10-mil Nb-25%Zr from two different suppliers. Also to be noticed is our variation in critical current for the same specimen on different occasions.

Part of the discrepancy, however, can be attributed to different sample lengths: our 12.5 m vs 1 cm for Young and Schenk and 95 cm for Taylor. "Current degradation," i.e., a coil critical (direct) current much below that expected from short sample performance (80), is a well-known phenomenon. This is a problem in dc applications; we expect it to

carry over to ac, probably in aggravated form. Insofar as our bifilar winding is not truly noninductive, some degradation may be expected.

It is tempting to think that critical current decreases with increased frequency because of heating due to ac loss (78, 81). But that should cause the plated wire to have a lower critical current than the bare wire, contrary to Fig. 30. Moreover, Rogers (82) has published results demonstrating that the 50-Hz transition is not in general a thermal process but is due rather to the peak current attaining a critical value. If so, the peak value must vary with frequency. Linford (83) has even reported a minimum and a maximum critical current at different nonzero frequencies for a particular thickness of niobium strip.

The critical dc is of interest because it is the single parameter of the hysteresis theory presented in Section II. The bare-wire value of 85 A shown in Fig. 30 for 19 April was the result of measurements made on that day. Fourteen values were recorded on four different days; as shown in Table 2, they ranged from 81.9 A through 90.0 A. (The output of our dc power supply was limited to 100 A, so we missed the first reading on 12 February. Later we obtained another, identical power supply and used the two in parallel to obtain the plated wire critical current.) Current was increased by hand control at a rate of about 2 A/sec. This rate, along with some jerkiness in the control probably resulted in transitions at currents somewhat lower than the true critical dc.

3. **AC Loss.** Figures 31 and 32 show the measured, bare-wire energy loss per cycle on 15 April and 19 April, respectively, at the three frequencies used. The theory of Section II predicts no loss below $I_m = I_{c1} \triangleq 2\pi R H_{c1}$. Assuming from work by Fietz (43)

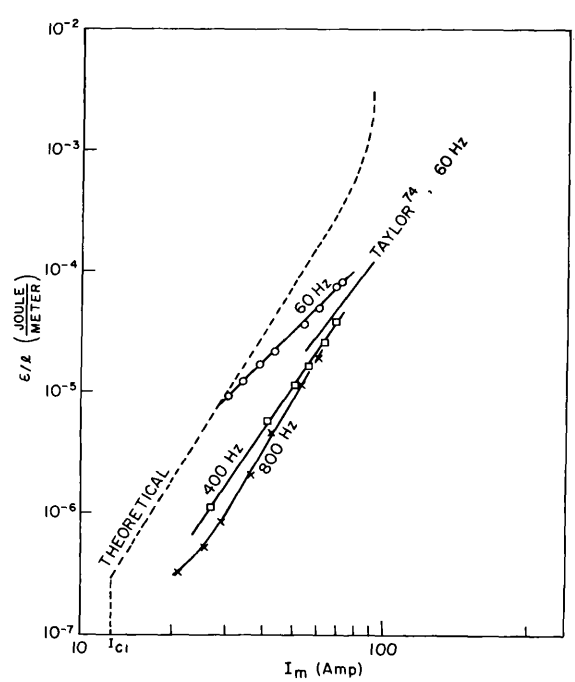

Fig. 31 – Bare wire energy loss per cycle (15 April data) versus current amplitude compared to the calculated hysteresis loss for a critical current of 90 A

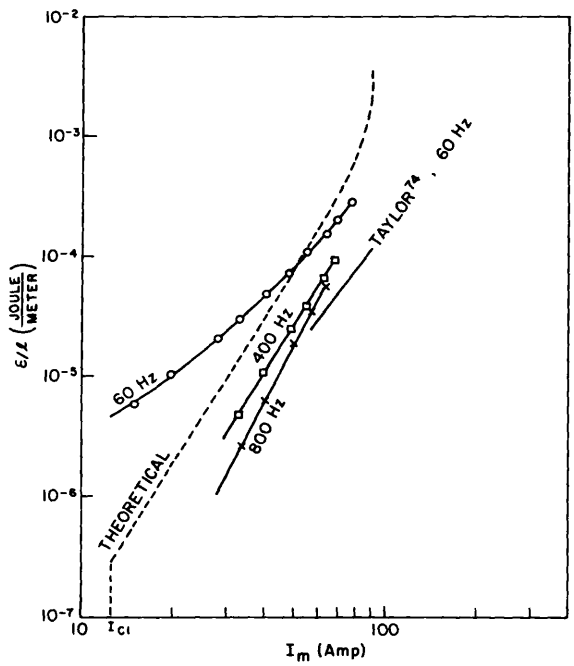

Fig. 32 – Bare wire energy loss per cycle (19 April data) versus current amplitude compared to the calculated hysteresis loss for a critical current of 90 A

that H_{c1} = 200 Oe, then I_{c1} = 12.7 A, which is just about where the loss becomes measurable. The theoretical hysteresis loss was calculated from Fig. 20 and is shown in Figs. 31 and 32 as a dotted line. We used the highest critical dc measured, on the assumption that the real critical dc is higher still. This is borne out by Figs. 31 and 32, which show that for the most part the measured loss is less than the hysteresis loss calculated for I_c = 90 A. A critical current of at least 260 A would be necessary to fit the 15 April data; we do not believe the actual critical dc can be that much greater than our measured values. The measured loss for the same specimen of bare wire differs by as much as ±50 percent under presumably the same experimental conditions. We do not know how to account for this; we can only suggest that surface conditions or trapped flux may have been different on the two occasions.

Also shown in Figs. 31 and 32 is a portion of Taylor's results (74). There is fair agreement with our 15 April data; but Taylor found no significant difference in the loss per cycle for the same current at 60 and 412 Hz, whereas we have the distinct curves shown in Figs. 31, 32, and 33 for 60, 400, and 800 Hz. We consistently find higher loss per cycle at a lower frequency for a given current amplitude, whereas the theory of Section II predicts a loss per cycle independent of frequency. This suggests that either the model used is deficient or an additional loss mechanism is involved. But if the latter, the measured loss should be higher than the predicted hysteresis loss rather than lower as found for the bare wire.

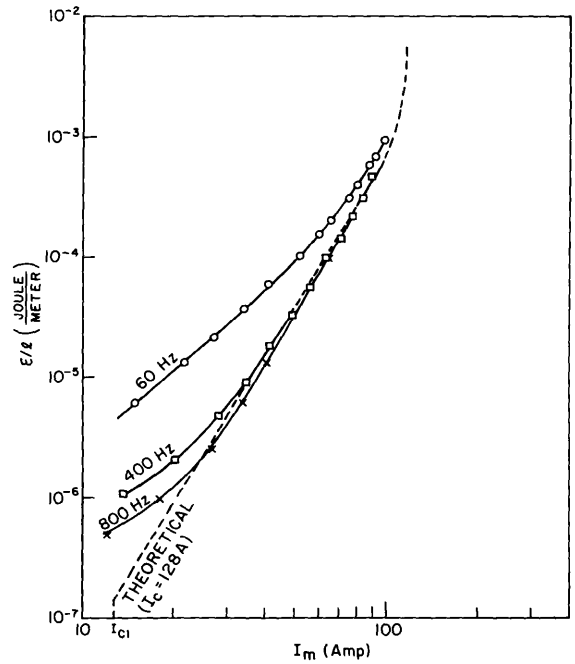

Fig. 33 – Plated wire energy loss per cycle versus current amplitude compared to the calculated hysteresis loss for a critical current at 128 A

Figure 33 shows the measured loss per cycle for the plated wire. It is slightly greater than that for the bare wire on 19 April and considerably greater than that for the bare wire on 15 April. As shown by the theoretical curve for I_c = 128 A, there is much better agreement between theory and experiment for the plated wire than for the bare wire, at least for the higher frequencies and currents. At low current the loss tends to be higher than that predicted by the critical state model; and the lower the frequency, the greater the divergence. A measured loss higher than the theoretical hysteresis loss would seem to support the additional-mechanism explanation. An additional mechanism that suggests itself is eddy currents in the normal fluid (Section I.D.1) of both bare and plated wires and in the copper sheath of the plated wire. While the plated wire does show an increased loss over that of the bare wire, the frequency dependence is wrong in both cases. An eddy-current power loss proportional to ω^2 would result in an energy loss per cycle that increased with frequency.

Although the energy loss per cycle decreases with frequency, the power loss does increase with frequency as shown in Figs. 34 and 35 for the bare and plated wires, respectively. Plots of effective resistivity versus rms current are shown in Fig. 36 and Fig. 37 for the bare wire and plated wire, respectively. We find a "worst-day" resistivity of 18 pΩ-cm (1.8×10^{-11} ohm-cm) at 60 Hz and 10 A rms compared to about 150 pΩ-cm (1.50×10^{-10}) for Zar (15) at 100 Hz and the same current, whereas Wisseman (16) reports approximately 3 fΩ-cm (3×10^{-15} ohm-cm) at 100 Hz and I_m = 8.14 A. According to Fig.

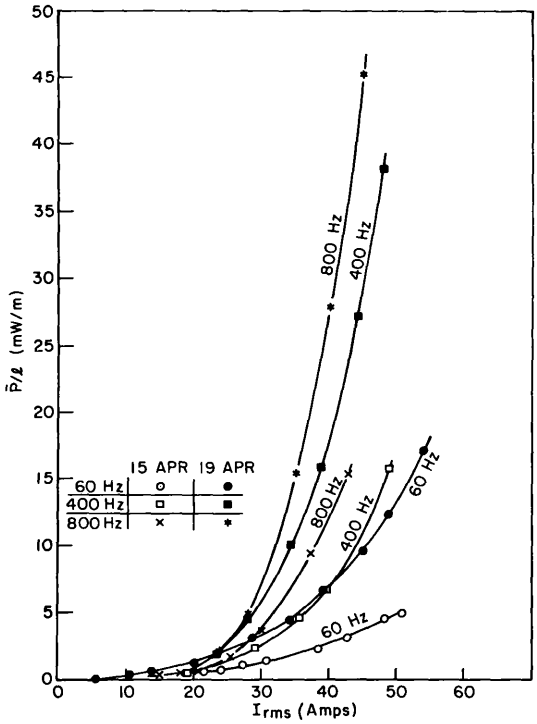

Fig. 34 – Bare wire loss versus effective current

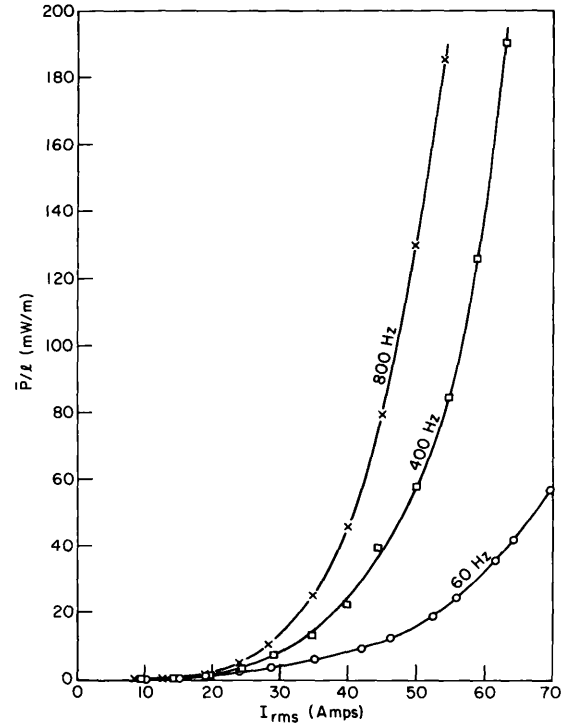

Fig. 35 – Plated wire power loss versus effective current

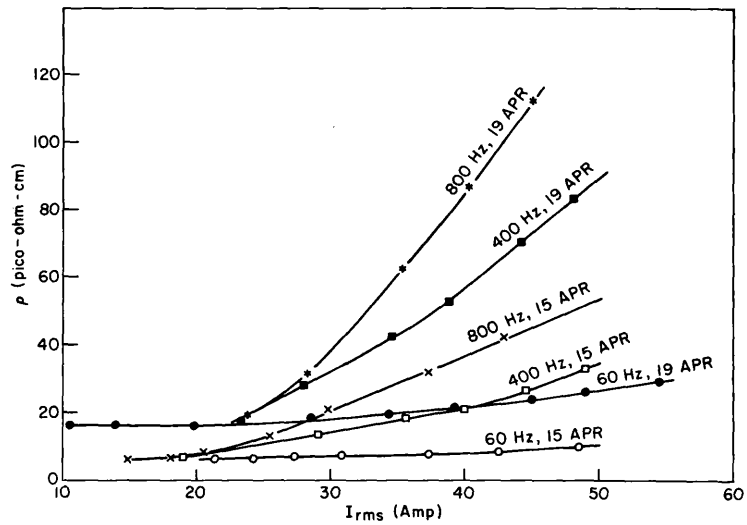

Fig. 36 – Bare wire effective resistivity versus effective current

36 we only approach Zar's value (on our worst day) at 800 Hz and more than 50 A rms. The extremely low resistivity found by Wisseman is probably due to his $I_m < I_{c1}$; i.e., his material probably never entered the mixed state.

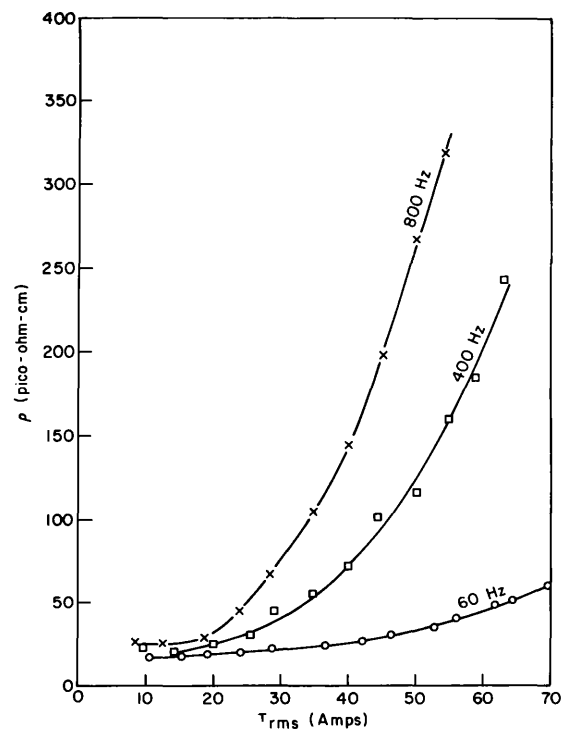

Fig. 37 – Plated wire effective resistivity versus effective current

Zar reports a resistivity independent of current over a range of 60 Hz to 30 kHz and 2 A to 30 A rms. That means a power loss proportional to I^2_{rms} and suggests an eddy-current rather than a hysteresis mechanism. Also, his 2 A is well below I_{c1}. Wisseman found the same loss for different current waveforms having the same peak value and therefore concluded that he was dealing with hysteresis. Close inspection of our Figs. 31, 32, and 36 reveals a tendency toward the eddy-current current dependence at 60 Hz but toward the hysteresis current dependence at 400 and 800 Hz.

The variation of bare-wire resistivity with frequency is shown in Fig. 38 for 50 A rms. At this current we find $\rho \propto f^{0.63}$, which may be compared to the $f^{0.6}$ reported by Jackson **(58)** over a range of 5 to 700 Hz. Our result is intermediate to Zar's $\rho \propto f^{1.7}$ for $f < 500$ Hz and $\rho \propto f^{0.5}$ for $f > 1$ kHz. Wisseman reports a hysteresis (i.e., linear) frequency dependence, but in view of the low current used, the effect encountered may be the type of surface hysteresis discussed by Buchhold (44). On the other hand, the linear dependence implied by Taylor (74) is based on currents up to 180 A peak.

An effective resistivity proportional to $f^{0.5}$ or $f^{0.6}$ suggests a skin effect. But the ac resistance of a normal wire (84) is proportional to $f^{0.5}$ only in the limit of very high frequency. At the power frequencies under consideration the ratio of (normal) ac to dc resistance for a wire of radius R is approximately

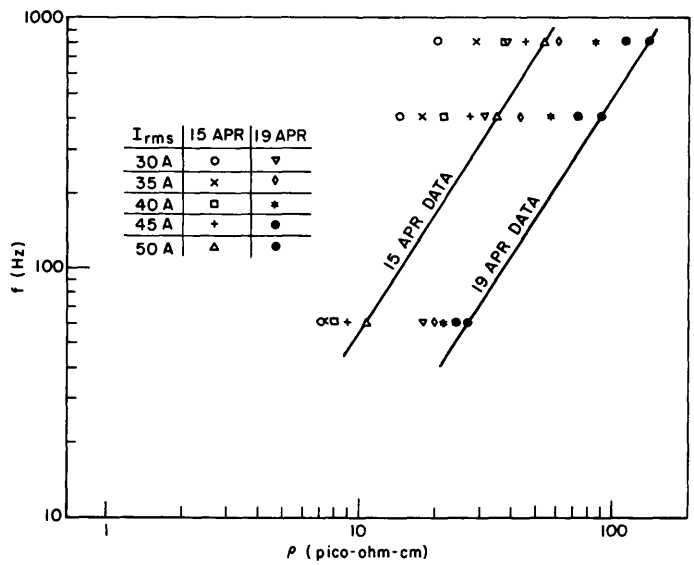

Fig. 38 – Bare wire effective resistivity versus frequency at an effective current of 50 A

$$\frac{R_n}{R_0} = 1 + \frac{1}{48} (\pi \mu \sigma f)^2 R^4, \tag{67}$$

where σ is the dc conductivity. We should be able to use this expression even at liquid helium temperatures; the anomalous skin effect (85) only begins to appear at microwave frequencies. Using Zar's value of 2.2 ohms as the normal resistance for a 45-cm long sample of 10-mil wire to obtain σ, it is easily seen that the second term of Eq. (67) is negligible compared to the first at our frequencies. In fact, the second term only equals the first at about 27 MHz. Thus we consider R_n in Eq. (3) to be independent of frequency; the f^2 dependence of R_{ac} in the eddy-current model is maintained for the frequencies of interest.

IV. CONCLUSIONS

We conclude that the ac loss of a type III superconductor at currents (or applied fields) such that it enters well into the mixed state is primarily due to hysteresis rather than eddy currents. This seems to be demonstrated by the waveforms in Fig. 28, in particular by the φ and I traces which are published here for the first time. Also, the $f^{0.63}$ frequency dependence of the power loss is closer to the linear dependence expected for hysteresis than to the f^2 dependence expected for an eddy-current loss.

The theory presented in Section II is the first application of the Riemersma model to a cylindrical superconductor carrying ac. It is clear from the discussion of experimental results in Section III that this theory is in general only qualitatively correct. For example, it predicts a power loss proportional to f rather than $f^{0.63}$. The theory is incomplete in that (even if the bulk hysteresis is due to a critical state approximated by $\mathbf{B} \times \mathbf{J} = \mathbf{C}$) there is no provision for surface hysteresis, for which there is accumulating evidence. Nevertheless the theory has engineering value in that it is simple and may be used for an estimate of the ac loss of a straight wire in its own field at power frequencies and at currents approaching the critical value. According to the experimental results of Section III, the estimate would be generally conservative for bare wire and quite close to actual losses for plated wire. Furthermore, the theory yields the first equivalent circuit proposed for the hysteresis loss of a superconductor.

As for ac power applications of superconductivity, these do not appear attractive for the sake of higher efficiency. According to Eq. (56), the theory predicts a high-current resistivity for 10-mil wire at 100 Hz that approaches 4×10^{-10} ohm-cm, independent of the particular type III material used. This is the order of resistivity reported by Zar which was deemed intolerable for efficient application in Section I. According to Eq. (52) if $I_m = I_c/10 > I_{c1}, \rho \approx 10^{-12}$ ohm-cm for the same frequency, which is more encouraging but which would not be efficient use of material. Experimental results lead us to the same conclusion. For 65 A rms at only 60 Hz, Fig. 35 has $\rho \approx 5 \times 10^{-11}$ ohm-cm, too high a resistivity for efficient application.

It might be thought that even if such conventional apparatus as rotating machinery and transformers, already highly efficient devices, cannot have their efficiencies (including that of a refrigerator) improved by economic application of superconductivity, the

low-voltage, static inverter would make a good application because of its relatively low efficiency. As mentioned in the Introduction, semiconductor switching devices have a voltage drop in the closed position that is significant at low input voltage, whereas an ideal superconducting switch would have no such drop. But a type III superconducting switch would have an ac loss – in addition to a normal-resistance loss in the open position.

Let us compare the cryotron loss to that of a certain 50-A transistor (MHT 2205) having a dissipation of about 5 watts when saturated; the cutoff loss is relatively negligible, and at our frequencies so is the switching loss. Consider an input voltage of 1 V and operation at 400 Hz. Then the loss per cycle of the transistor switch is 6.25 mJ. Let us use a length of 10-mil, Nb-25%Zr wire sufficient to give a normal resistance of 10 ohms for the gate winding. Assuming a normal resistance of 5 ohm/m based on Zar's report, the gate winding will be 2 m long. That gives an open-position loss of 125 μJ for 400 Hz. Using the 400 Hz curve in Fig. 32 for $I_m = 50$ A, we find that $\epsilon/\ell = 2.7 \times 10^{-5}$ J/m, which gives a switching loss of 2.7×10^{-5} J for a half cycle. Neglecting the ac loss in the control winding, we have a superconducting switch loss of 152 μJ per cycle compared to 6.25 mJ for the transistor switch. Thus, in light of the refrigeration requirements outlined in Section I a superconducting inverter is also economically unattractive.

It seems that for both the usual type of ac machine and for a static inverter, the efficiency gained by the use of a type III superconductor does not offset the inefficiency of a liquid-helium refrigerator. Others (86) apparently feel the same way about superconducting lines for ac transmission. We conclude that the prospects for economical application of superconductivity to continuous energy conversion processes involving ac are exceedingly dim, at least with present materials. If new superconductors are developed that either have significantly higher transition temperatures or do not have serious ac loss in the presence of high magnetic fields, then the question will be reopened.

With regard to power applications of superconductivity there remain then only dc applications and special ac applications where size is more important than efficiency as possibly worthwhile. The use of superconductors for dc transmission has been seriously proposed (86). The usual type of dc machine is inherently an ac machine (with a mechanical rectifier) and therefore not a good prospect, but the application of superconductivity to homopolar machines is worth considering. Dc energy storage is a promising area of application (87). Indeed, high-field magnets are an example of energy storage and are the only successful high-energy applications of superconductivity to date. But there is also a growing need for large-scale energy storage for discharge into pulse

power devices such as high-energy radars, sonars, and lasers. The discharge rates involved in such applications make an understanding of the ac behavior of high-field superconductors quite important for engineering design. The theory and equivalent circuit presented here may find some use in this endeavor.

The theory can be improved by including hysteresis due to the recently discovered superconducting sheath (21). A surface-flux-pinning model by Hart and Swartz (88) might be the place to start. The theory can be made more complete by incorporating the effect of a normal fluid in the penetration region. The eddy current and skin effect treatments that have appeared to date (13, 15, 39, 89) are not directly applicable to a type II or III superconductor in the mixed state. Practical design would also call for extension of the theory to deal with more complex geometries than that treated here. The current degradation effect referred to in Section III.D.2 is not even understood for dc. The same thing may be said for the associated phenomenon called flux jumping (23) and the general problem of stability. There are many gaps in our scientific understanding of high-field superconductors, but applications may proceed on the basis of a phenomenological approach such as the one employed here.

APPENDIX A

LIMITING VALUES OF THE LOSS EXPRESSION

1. $I_m/I_c \to 0$

As y approaches zero in Eq. (46), x does also, and the small-angle approximation may be used. The integral becomes

$$\mathcal{J}_A = \int_0^y \left[2x^3 + \frac{x^2}{\sqrt{2}} \left(\sqrt{y^2 - x^2} - \sqrt{y^2 + x^2} \right) \right] dx. \tag{A1}$$

Using Dwight (90) 232.01 and 352.01, we find

$$\mathcal{J}_A = \frac{y^4}{8} \left[1 + \frac{\pi}{2\sqrt{2}} + \frac{\ln\left(1 + \sqrt{2}\right)}{\sqrt{2}} \right]. \tag{A2}$$

And

$$\epsilon = \frac{\mu_0 \ell}{12\pi} \left[1 + \frac{\pi}{2\sqrt{2}} + \frac{\ln\left(1 + \sqrt{2}\right)}{\sqrt{2}} \right] \frac{I_m^{\,4}}{I_c^{\,2}}, \tag{A3}$$

which agrees rather well with the slope of the low-current curve in Fig. 20. The loss per unit length is

$$\frac{\epsilon}{\ell} = 0.912 \times 10^{-7} \frac{I_m^{\,4}}{I_c^{\,2}} \frac{\text{joule}}{\text{meter}}. \tag{A4}$$

2. $I_m = I_c$

When y = 1, the integral in Eq. (46) can be evaluated in closed form as follows:

$$\mathcal{J}_A = \int_0^1 \left[\frac{\arcsin x + \arg\tanh 1/\sqrt{2}}{\sqrt{1 - x^2}} + \frac{\arg\sinh x - \arg\tanh 1/\sqrt{2}}{\sqrt{1 + x^2}} \right] x^2\, dx. \tag{A5}$$

For the arcsin and arg sinh terms let x = sin Z and sinh Z, respectively. Then, using Dwight 430.21, 322.01, 671.21, and 202.01 for the four terms, respectively, we find

$$\mathcal{J}_A = \left[\frac{\pi^2}{16} + \frac{1}{4}\right] + \left[\frac{\pi}{4} \ln\left(1 + \sqrt{2}\right)\right] + \left[\frac{\ln\left(1 + \sqrt{2}\right)}{\sqrt{2}} - \frac{1}{4} - \frac{\ln^2\left(1 + \sqrt{2}\right.}{4}\right]$$

$$- \frac{\ln\left(1 + \sqrt{2}\right)}{2}\left[\sqrt{2} - \ln\left(1 + \sqrt{2}\right)\right] \tag{A6}$$

$$= \frac{1}{4}\left[\frac{\pi}{2} + \ln\left(1 + \sqrt{2}\right)\right]^2 \tag{A7}$$

or

$$\mathcal{J}_A = 1.503. \tag{A8}$$

The loss per unit length is

$$\frac{\epsilon}{\ell} = 4.01 \times 10^{-7}\, I_c^2\, \frac{\text{joule}}{\text{meter}}. \tag{A9}$$

APPENDIX B
THREE KINDS OF INDUCTANCE

The circuit form of Faraday's law is

$$V = \dot{\psi}, \tag{B1}$$

where ψ denotes flux linkages. In the self-field case

$$V = \frac{d\psi}{dI}\,\dot{I}. \tag{B2}$$

The incremental or dynamic self inductance (51) is defined as

$$L_d \triangleq \frac{d\psi}{dI}\,. \tag{B3}$$

In light of Eq. (B2) the incremental inductances are easily found from the voltage equations already presented. For example, during the initial excitation Eq. (26) gives

$$L_d = \frac{\mu_0 \ell}{3\pi}\,\frac{I}{\sqrt{I_c^2 - I^2}}\,\arctan\frac{I}{\sqrt{I_c^2 - I^2}}\,, \tag{B4}$$

where $2\pi R H_{c1} < I \leq I_c$. While the incremental inductance is usually the most useful in nonlinear circuit theory – because of the simple form of Eq. (B2) in terms of L_d – and yields the most simple expressions in our case, we prefer the absolute inductance (51):

$$L_a \triangleq \frac{\psi}{I}\,. \tag{B5}$$

Comparing the general equation Eq. (B1), with our special equation, Eq. (20), shows that we have

$$\varphi = \psi = L_a\, I. \tag{B6}$$

The advantage of the absolute inductance in our case is that it directly relates flux to current. This gives more insight into magnetic conditions in the superconductor.

According to Eq. (B6), L_a may be found by integrating our B equations and dividing by I. The solution is outlined for the initial excitation. From Eq. (22)

$$\varphi(\rho) = \ell \sqrt{\frac{2}{3}\mu_0 C} \int_{\rho}^{R} \sqrt{r - \frac{\rho^3}{r^2}}\, dr \triangleq k_B \mathcal{J}_B. \tag{B7}$$

Typical of most integrals encountered with this model, $\mathcal{J}_B$ is of the form

$$\mathcal{J} = \int x^m (a + bx^n)^p \, dx,$$

where m, n, and p are rational numbers. Integrals of this form can be expressed in terms of elementary functions in certain cases (91). The substitution $x^n = z$ gives

$$\mathcal{J}_B = \frac{1}{3} \int \frac{\sqrt{a + bz}}{z} \, dz \tag{B8}$$

and, using Dwight (90) 194.11, leads to

$$\varphi = \frac{\mu_0 \ell}{3\pi} \left[I - \sqrt{I_c^2 - I^2} \arctan \frac{I}{\sqrt{I_c^2 - I^2}} \right], \tag{B9}$$

where $2\pi R H_{c1} < I \leq I_c$. The absolute inductance is, therefore,

$$L_a = \frac{\mu_0 \ell}{3\pi} \left[1 - \frac{\sqrt{I_c^2 - I^2}}{I} \arctan \frac{I}{\sqrt{I_c^2 - I^2}} \right] \tag{B10}$$

for the same range of I. Values for other ranges are given in Table 1.

Whereas the incremental inductance is defined so that

$$V = L_d \dot{I}, \tag{B11}$$

the definition of absolute inductance is such that

$$V = L_a \dot{I} + I \dot{L}_a. \tag{B12}$$

According to Eq. (B4) the incremental inductance increases without limit as I approaches I_c, but Eq. (B10) gives

$$L_a \xrightarrow[I \to I_c]{} \frac{\mu_0 \ell}{3\pi}. \tag{B13}$$

This is somewhat larger than the internal inductance of a normal conductor (52):

$$L_i = \frac{\mu_0 \ell}{8\pi}. \tag{B14}$$

Consider two conductors of the same radius, one normal and the other superconducting, carrying the same current I_c. Their magnetic fields must be the same at the surface, but whereas the field variation within the normal conductor is linear, that within the superconductor, according to Eq. (11), varies as $r^{1/2}$. Thus the critical superconductor will contain more flux. Moreover, flux linkages for the normal conductor will be only half the value of its flux.

Another possible definition of inductance is in terms of the magnetic energy (92):

$$\epsilon_m \triangleq \frac{L_\epsilon I^2}{2}. \tag{B15}$$

But here

$$\epsilon_m = \int \mathbf{H} \cdot d\mathbf{B}\, d\tau = \frac{1}{2\mu_0} \int B^2\, d\tau, \tag{B16}$$

where the integration is to be carried out over the volume of the wire. For example, during the initial excitation, using Eq. (11),

$$L_\epsilon = \frac{4\pi C\ell}{3I^2} \int_\rho^R \left(r^2 - \frac{\rho^3}{r}\right) dr, \tag{B17}$$

which leads to

$$L_\epsilon = \frac{\mu_0 \ell}{6\pi} \left[1 + \left(\frac{I_c^2 - I^2}{I^2}\right) \ln \left(\frac{I_c^2 - I^2}{I_c^2}\right)\right], \tag{B18}$$

where $2\pi R H_{c1} < I \leq I_c$. Equation (B18) is not only functionally different from Eq. (B10), it has a different upper limit:

$$L_\epsilon \xrightarrow[I \to I_c]{} \frac{\mu_0 \ell}{6\pi}. \tag{B19}$$

Thus the three kinds of inductance are quite different; which one should be used, if any, is a matter of taste or convenience.

APPENDIX C
SPECIMEN INDUCTANCE

The total self inductance of a specimen was calculated by the methods of Grover (93). The bifilar winding of a specimen is assumed to consist of two single-layer coils intertwined and connected in series opposition. Wire is of diameter 2R = 10 mils wound on a former of length b = 8 in. and radius a = 1.25 in. The pitch of each winding is P = 0.25 in.; the number of turns is N = b/P = 32.

For a helix of round wire Grover's Eq. (135) has

$$L = L_s - 0.004\pi aN\,(G + H), \tag{C1}$$

where L_s is the inductance (in μH for a in cm) of a cylindrical current sheet of length b and diameter 2a. The quantities G and H combine to give a correction term for insulating space; G is given by his Eq. (136):

$$G = \frac{5}{4} - \ln\frac{P}{R} = -2.66, \tag{C2}$$

and for 32 turns his Table 39 has H = 0.3095. The inductance L_s is found from Nagaoka's formula, Grover's Eq. (118):

$$L_s = 0.002\pi^2 a \left(\frac{2a}{b}\right) N^2 K, \tag{C3}$$

where K is a correction factor for end effects. For long coils, i.e., b > 2a, Grover's Table 37 is used, and K = 0.879. Thus L_s = 17.7 μH and L_1 = 20.7 μH for either of the two assumed coils.

To obtain the mutual inductance between the two, Grover's Eq. (110) for concentric coaxial coils of the same length is used:

$$M = 0.004\pi^2 a^2 n_1 n_2 \,[r_1 B_1 - AB_2]. \tag{C4}$$

Here n_1 and n_2 are winding densities, r_1 is the diagonal given by $r_1^2 = a^2 + b^2$, A = a, and the B's are given by his Table 29. We have $n_1 = n_2 = N/b = 1/P = 4$/in. and r_1 = 8.10 in. The table gives $B_1 = 1$ and $B_2 = 0.848$, so M_{12} = 17.6 μH. Then $L_x = 2(L_1 - M_{12})$ = 6.2 μH, to which we add the internal inductance given by Eq. (59):

$$L_i = \frac{\mu_0 \ell}{8\pi} = 0.6\ \mu\text{H}. \tag{C5}$$

The resulting self inductance of the specimen is 6.8 μH.

The inductance of a copper-clad specimen was measured on a General Radio type 1632-A inductance bridge and found to be 7.2 μH at 400 Hz. This involved a somewhat dubious correction for the inductance of the leads. A more direct measure was obtained from a V_s trace taken during the nulling routine. This gave 7.1 μH at about 0.5 A and 800 Hz for the bare specimen.

WORKS CITED

1. E. A. Lynton, *Superconductivity*, New York, Wiley, 1962
2. J. E. Kunzler, E. Buehler, F. S. L. Hsu, and J. H. Wernick, *Phys. Rev. Ltrs.* **6**, 39 (1961)
3. R. McFee, *Elec. Engng.* **81**, 122 (1962)
4. J. H. Kuhlmann, *Design of Electrical Apparatus*, 2 edition, New York, Wiley, 1940
5. A. Still, *Elements of Electrical Design*, 2 edition, New York, McGraw-Hill, 1932
6. J. E. Kunzler, *Rev. Mod. Phys.* **33**, 501 (1961)
7. E. G. Frankel, J. M. Reynolds, and E. H. Sibley, *Naval Engineers J.* **78**, 501 (1966)
8. J. W. Angrist, *Direct Energy Conversion*, Boston, Allyn and Bacon, 1965; K. H. Spring, *Direct Generation of Electricity*, New York, Academic Press, 1965; G. W. Sutton, *Direct Energy Conversion*, New York, McGraw-Hill, 1966
9. B. D. Bedford and R. G. Holt, *Principles of Inverter Circuits*, New York, Wiley, 1964
10. D. J. Hanrahan, *IRE Trans Ed-9*, 358 (1962)
11. T. Roddam, *Transistor Inverters and Converters*, Princeton, Van Nostrand, 1963
12. D. A. Buck, *Proc. IRE* **44**, 482 (1956)
13. D. Shoenberg, *Superconductivity*, Cambridge University Press, 1952
14. J. M. Rayroux, *Brown Boveri Rev.* **53**, 42 (1966)
15. J. L. Zar, *J. Appl. Phys.* **35**, 1610 (1964)
16. W. R. Wisseman, L. A. Boatner, and F. J. Low, *J. Appl. Phys.* **35**, 2649 (1964)
17. H. Riemersma, *J. Appl. Phys.* **35**, 1802 (1964)
18. D. B. Montgomery, *IEEE Spectrum* **1**, 103 (1964); C. Laverick, *IEEE Spectrum* **5**, 63 (1968)

19. B. W. Roberts, *Superconductive Materials and Some of Their Properties*, General Electric Report 63-RL-3252M, 1963

20. Y. B. Kim, C. F. Hempstead, and R. A. Strnad, *Phys. Rev.* **131**, 2486 (1963)

21. P. G. deGennes, *Superconductivity of Metals and Alloys*, New York, Benjamin, 1966

22. R. A. Kamper, *Phys. Ltrs.* **5**, 9 (1963); W. Klose, *Phys. Ltrs.* **8**, 12 (1964)

23. J. Lowell, *Cryogenics* **5**, 185 (1965)

24. K. Mendelssohn and J. R. Moore, *Proc. Roy, Soc.* **A151**, 334 (1935)

25. C. P. Bean, *Phys. Rev. Ltrs.* **8**, 250 (1962); *Rev. Mod. Phys.* **36**, 31 (1964)

26. Lord Rayleigh, *Phil. Mag.* **5**, 23 (1887)

27. C. P. Bean and R. W. Schmitt, *Sci.* **140**, 26 (1965)

28. F. J. Morin, J. P. Marita, H. J. Williams, R. C. Sherwood, J. H. Wernick, and J. E. Kunzler, *Phys. Rev. Ltrs.* **8**, 275 (1962)

29. A. A. Abrikosov, *Sov. Phys. JETP* **5**, 1147 (1957)

30. B. B. Goodman, *Phys. Rev. Ltrs.* **6**, 597 (1961)

31. J. M. Blatt, *Theory of Superconductivity*, New York, Academic Press, 1964

32. P. W. Anderson and Y. B. Kim, *Rev. Mod. Phys.* **36**, 39 (1964)

33. P. W. Anderson, *Phys. Rev. Ltrs.* **9**, 309 (1962)

34. Y. B. Kim, C. F. Hempstead, and A. R. Strnad, *Phys. Rev. Ltrs.* **9**, 306 (1962)

35. Y. B. Kim, C. F. Hempstead, and A. R. Strnad, *Phys. Rev.* **139**, A1163 (1965)

36. R. B. Jones, E. H. Rhoderick and A. C. Rose-Innes, *Phys. Ltrs.* **15**, 214; B. D. Josephson, *Phys. Ltrs.* **16**, 242; H. O. Lorch, *Phys. Ltrs.* **17**, 196; R. H. Romer, *Phys. Ltrs.* **17**, 223 (1965); J. G. Park, *Phys. Ltrs.* **20**, 346 (1966)

37. I. Giaever, *Phys. Rev. Ltrs.* **15**, 825 (1965); P. R. Solomon, *Phys. Rev. Ltrs.* **16**, 50; I. Giaever, *Phys. Rev. Ltrs.* **16**, 460 (1966)

38. D. J. Quinn, III, and W. B. Iffner, III, *J. Appl. Phys.* **33**, 748 (1962)

39. F. London, *Superfluids*, Vol. I, New York, Dover, 1960

40. R. E. Glover and M. Tinkham, *Phys. Rev.* **108**, 243 (1957)

41. J. Bardeen, L. N. Cooper, and J. R. Schrieffer, *Phys. Rev.* **108**, 1175 (1957)

42. H. London, *Phys. Ltrs.* 6, 162 (1963)

43. W. A. Fietz, M. R. Beasley, J. Silcox, and W. W. Webb, *Phys. Rev.* **136**, A335 (1964)

44. T. A. Buchhold, *Cryogenics* 3, 141 (1963)

45. P. S. Swartz and H. R. Hart, Jr., *Phys. Rev.* 137, A818 (1965)

46. R. M. Easson and P. Hlawiczka, *Brit. J. Appl. Phys.* **18**, 1237 (1967); B. Bertman and D. G. Schweitzer, *Phys. Ltrs.* **21**, 361; K. G. Carroll, *Phys. Ltrs.* **23**, 416 (1966); H. A. Ullmaier and W. F. Gauster, *J. Appl. Phys.* **37**, 4519 (1966)

47. T. W. Grasmehr, Ph.D. dissertation, Elec. Engr. Dept., Carnegie Inst. of Tech., Pittsburgh, Pa., 1965

48. H. F. Taylor, *Bull. Am. Phys. Soc.* 12, 520 (1967)

49. I. S. Sokolnikoff, *Advanced Calculus*, New York, McGraw-Hill, 1939

50. D. J. Hanrahan and H. E. Stockman *Proc. IRE* **50**, 1844 (1962)

51. W. L. Hughes, *Nonlinear Electrical Networks*, New York, Ronald Press, 1960

52. E. Weber, *Electromagnetic Fields*, New York, Wiley, 1950

53. A. D. Anderson, W. R. Roach, and R. E. Sarwinski, *Rev. Sci. Instr.* **37**, 1024 (1966)

54. T. A. Buchhold and P. J. Molenda, *Cryogenics* 2, 344 (1962)

55. M. L. Claude and M. A. Mailfert, *Phys. Ltrs.* **24A**, 150 (1967)

56. B. B. Figgins and I. A. Shepherd, *Nature* **202**, 890 (1964)

57. C. Grenier and B. Elschner, *Philips Res. Rpts.* **20**, 235 (1965)

58. W. D. Jackson and A. N. Chandra, *MIT Qtr. Prog. Rpt.* 75, 1964

59. C. H. Jones and H. L. Schenk, *Advan. Cryo. Engr.* **8**, 579, New York, Plenum Press (1963)

60. R. A. Kamper and P. F. Chester, *Proc. 8th Intr. Conf. Low Temp. Phys.* 371, London, Butterworth's, 1963

61. T. Pech and G. Fournet, *Cryogenics* 7, 26 (1967)

62. R. G. Rhodes, E. C. Rogers, and R. J. A. Seebold, *Cryogenics* **4**, 206 (1964)

63. Y. A. Rocher and J. Septfonds, *Cryogenics* **7**, 96 (1967)

64. R. J. Slaughter, E. C. Rogers, and R. Grigsby, *Phys. Ltrs.* **23**, 214 (1966)

65. M. P. Thomas, *Bul. Soc. Franc. Elect.* **5**, 633 (1964)

66. J. R. Birchak, M. A. Thesis, Rice U., Houston, Texas, 1964

67. G. Bogner and W. Heinzel, *Solid-State Electr.* **7**, 93 (1964)

68. R. M. Easson and P. Hlawiczka, *Brit. J. Appl. Phys.* **18**, 1237 (1967)

69. K. Hidaka, H. Miyata, K. Shinada, S. Ihara, and T. Sekine, *Tokyo Electrotech. Lab. Bul.* **28**, 1 (1964)

70. W. Heinzel, *Phys. Ltrs.* **20**, 260 (1966)

71. R. A. Kamper, *Phys. Ltrs.* **2**, 290 (1962)

72. T. Pech, J. P. Duflot, and G. Fournet, *Phys. Ltrs.* **16**, 201 (1965)

73. H. F. Taylor, *Appl. Phys. Ltrs.* **11**, 169 (1967)

74. H. F. Taylor, *Phys. Rev.* **165**, 517 (1968)

75. H. Voigt, *Phys. Ltrs.* **20**, 262 (1966)

76. H. A. Ullmaier, *Phys. Stat. Sol.* **17**, 631 (1966)

77. C. F. S. Malseed, R. B. Nethercott, and W. A. Rachinger, *Phys. Ltrs.* **22**, 551 (1966)

78. F. J. Young and H. L. Schenk, *J. Appl. Phys.* **35**, 980 (1964)

79. E. C. Rogers, *Phys. Ltrs.* **5**, 317 (1963)

80. J. K. Hahn, B. S. Chandrasekhar, and H. Riemersma, *Advan. Cryo. Engr.* **8**, 17, New York, Plenum Press (1963)

81. R. M. Easson, P. Hlawiczka, and J. M. Ross, *Phys. Ltrs.* **20**, 465 (1966)

82. E. C. Rogers, *Phys. Ltrs.* **22**, 365 (1966)

83. R. M. F. Linford, *Phys. Ltrs.* **17**, 18 (1965)

84. A. Sommerfeld, *Electrodynamics*, New York, Academic Press, 1952

85. C. Kittel, *Introduction to Solid State Physics*, 3rd ed., New York, Wiley, 1967

86. R. L. Garwin and J. Mitisoo, *Proc. IEEE* **55**, 538 (1967)

87. E. J. Lucas, Z. J. J. Stekly, A. Foldes, and R. A. Milton, *IEEE Trans. Mag.* **MAG-3**, 280 (1967)

88. H. R. Hart, Jr., and P. S. Swartz, *Phys. Rev.* **156**, 403 (1967)

89. H. B. G. Casimir and J. Ubbink, *Philips Tech. Rev.* **28**, 271 (1967)

90. H. B. Dwight, *Tables of Integrals and Other Mathematical Data*, 3rd ed., New York, MacMillan, 1957

91. I. S. Gradshteyn and I. M. Ryzhik, *Table of Integrals, Series, and Products*, New York, Academic Press, 1965

92. W. K. H. Panofsky and M. Phillips, *Classical Electricity and Magnetism*, Cambridge, Addison-Wesley, 1955

93. F. W. Grover, *Inductance Calculations*, New York, Van Nostrand, 1946

UNCLASSIFIED
Security Classification

DOCUMENT CONTROL DATA - R & D

(Security classification of title, body of abstract and indexing annotation must be entered when the overall report is classified)

1. ORIGINATING ACTIVITY *(Corporate author)* Naval Research Laboratory Washington, D. C. 20390	2a. REPORT SECURITY CLASSIFICATION Unclassified 2b. GROUP

3. REPORT TITLE

A THEORETICAL AND EXPERIMENTAL STUDY OF THE AC LOSSES OF A HIGH FIELD SUPERCONDUCTOR AND THE IMPLICATIONS FOR POWER APPLICATIONS

4. DESCRIPTIVE NOTES *(Type of report and inclusive dates)*
A final report

5. AUTHOR(S) *(First name, middle initial, last name)*

Donald J. Hanrahan

6. REPORT DATE February 26, 1969	7a. TOTAL NO. OF PAGES 66	7b. NO. OF REFS 93

8a. CONTRACT OR GRANT NO. NRL Problem E01-01 b. PROJECT NO. RR 010-04-41-5950 c. SR 007-12-01-0800 d.	9a. ORIGINATOR'S REPORT NUMBER(S) NRL Report 6820 9b. OTHER REPORT NO(S) *(Any other numbers that may be assigned this report)*

10. DISTRIBUTION STATEMENT

This document has been approved for public release and sale; its distribution is unlimited.

11. SUPPLEMENTARY NOTES	12. SPONSORING MILITARY ACTIVITY Department of the Navy (Office of Naval Research), Washington, D. C. 20360

13. ABSTRACT

A theory for the hysteresis loss of a high-field superconductor carrying ac is presented, based on the Riemersma critical state model ($\mathbf{B} \times \mathbf{J} = \mathbf{C}$). Voltage waveforms, energy loss per cycle, and limiting values of effective resistivity are derived. For sinusoidal current of frequency f in 10-mil wire the high (critical) current limit of resistivity is found to be $4.06 \cdot 10^{-14}$ f (ohm-meter) compared to $0.93 \cdot 10^{-16}$ f for a current peak of one-tenth the critical current; both values are independent of the high-field material used. An equivalent circuit consisting of a variable inductance is proposed for the hysteretic superconductor and three possible definitions of the inductance are discussed. In any case, the inductance is nonlinear, a transcendental function of the current, the function being different on the four segments of a hysteresis loop. The high-current limit of the absolute, internal inductance (the preferred definition) per unit length is $\mu_0/3\pi$ (henry/meter).

Experiments were performed at 4.2°K on bifilar windings of 10-mil, Nb25%Zr wire, both bare and copper plated. Currents up to the critical value were used at frequencies of 60, 400, and 800 Hz. A compensation technique was employed to obtain the voltage due to internal magnetic field; oscillograms of the corresponding volt-amp characteristic and of various waveforms were made. Current and compensated voltage waveforms were used to calculate the loss per cycle. Oscillograms were in fair agreement with theoretical waveforms. Critical currents decreased with frequency, and the copper-plated wire had consistently higher values than the bare wire, although losses were higher for the copper-plated wire. There was some quantitative agreement between the experimental plated-wire loss and that calculated from the theory, but the measured bare-wire loss was generally less than that predicted by the theory, based on a

(Continued)

DD FORM 1 NOV 65 1473 (PAGE 1)
S/N 0101-807-6801

UNCLASSIFIED
Security Classification

14. KEY WORDS	LINK A ROLE	LINK A WT	LINK B ROLE	LINK B WT	LINK C ROLE	LINK C WT
Superconductivity						
Energy conversion						
Electrical resistance						
Core loss						
Hysteresis						
Electric power						
Electric machinery						
Energy processing						
Energy storage						

Abstract (continued)

measured critical current. The effective resistivity was found to vary as $f^{0.63}$, which fits neither an eddy-current theory nor the simple hysteresis model used. Experimental values of resistivity agree more with Zar than with Wisseman. The theory gives a generally conservative estimate of the ac loss, useful for engineering purposes.

The feasibility of applying superconductivity to two classes of ac power equipment is discussed: (1) conventional apparatus such as transformers and rotating machines, already highly efficient, and (2) low-voltage static inverters which are not so efficient. A novel circuit is presented for a superconducting inverter or oscillator. We conclude in both cases that, although the superconducting device is more efficient than its room-temperature counterpart, the inefficiency of liquid-helium refrigeration precludes economical application of superconductivity. Unless new materials are developed that have either significantly higher transition temperatures or much less ac loss under high field conditions, the prospects for continuous ac power applications of superconductivity are bleak. There is still some promise for dc power applications and dc energy storage for discharge into pulse power devices.